Foil fluorescence in MARS spectral imaging

A thesis submitted in partial fulfilment
of the requirements for the
Master of Science in Medical Physics
at the
University of Canterbury

---

by

Lieza Vanden Broeke

May 2015

Abstract

This thesis details work in developing an optimised model for the energy calibration of a Medipix All Resolution System (MARS) multi-energy computed tomography (spectral CT) scanner. The main motivation behind this research came from an unpublished internal document titled "Using Beer's law in MARS scanners" which challenged the current image reconstruction process. The document required an accurate per-pixel understanding of each of the components of the MARS scanner. The objective of my research was to work as part of the "foil group" to optimise the per-pixel energy calibration technique of the MARS multi-energy scanner using the x-ray fluorescence (XRF) technique originally worked on by Raj Kumar Panta (University of Otago). The emission of XRF is generated from the interaction between an x-ray beam and a high atomic number target. The main modification made to Panta's method in this research was to measure the XRF found outside of the primary x-ray beam. This modification aimed to increase the ratio of XRF to background photons remaining from the polychromatic x-ray beam. Initial testing of the method, however, did not consistently detect the XRF for the molybdenum and tantalum foils. Their XRF peaks were not well-defined and not consistent across the pixels. The lead XRF peak from the lead foil was clear and well-defined in each pixel.

This led into an investigation for optimising the thickness of the foils used to ensure that maximum fluorescence is escaping the foil. Two stages of the model were developed: (1) assumes a monochromatic beam and calculates the optimum thickness based in the effective energy of the beam; and (2) assumes a polychromatic beam where the optimum foil thickness is calculated through numerical integration. The energy integrating model suggests a foil thickness of 50 μm for molybdenum, 100 μm for indium, and 210 μm for lead. The results suggest that initial testing of the XRF method used sub-optimal foil thicknesses, explaining the low fluorescence signal.

The optimal foil thickness model is being used to plan the next stage of experiments that the foil group will perform. The validity of the energy integrating model will be checked and the modified XRF technique described in this research will be automated so that minimal user intervention is required for performing the XRF energy calibration. The work in this thesis has contributed to two refereed publications. The improved energy calibration improves the image reconstruction and gives more accurate images, bringing the MARS team closer to their five-year visionary goal of extending the concept of multi-energy CT into human imaging.

Acknowledgements

I would like to thank Prof. Phil Butler, Assoc. Prof. Anthony Butler, Dr. Stephen Bell, and Dr. Steven Marsh for supervising my masters study. I am incredibly grateful for all the encouragement they have provided throughout the year. I am also very appreciative of the financial support the MARS group has given me.

Working with the MARS group has been an amazing opportunity. I have always been inquisitive by nature and everyone in the group was always happy to answer my questions. In fact, my questions were encouraged. The passion they show for the work they do is exceptional. I am so grateful for having had the opportunity to work alongside them and would like to thank all the members of the MARS team for their help and support in completing this thesis.

Particular mention must be made to Brian Goulter, Joe Healy, Ali Atharifard and Mohsen Ramyar. As a part of the foil group many valuable discussions were had and helpful advice was always given. Christopher Bateman has also been a huge help in getting this thesis written. He has made an enormous effort to proof read this thesis, and his encouragement has given me the passion and drive to pursue further study.

Finally I would like to express my love and gratitude to my family and friends who have shown me infallible support during my studies. Special mention must be made to my parents and sisters for believing in me every step of the way, to my horse Bamboozle for keeping me sane, and to Ben Bosomworth for always managing to make me smile.

Contents

Chapter 1

Introduction to the thesis

This thesis details work contributing to the development of a precise per-pixel energy calibration method for the Medipix All Resolution System (MARS) using metal foil fluorescence. The work in this thesis is broken into two parts: (1) a preliminary method and associated experiments for detecting fluorescence with MARS; and (2) a theoretical model developed for optimising the foil thickness used in the preliminary method to maximise the detected fluorescence signal.

A previous technique for calibrating the energy response of the MARS detector using x-ray fluorescence (XRF) generated by directly irradiating metallic targets with x-rays was developed by Panta *et. al.* [1]. In the XRF technique a polychromatic x-ray beam is directed towards these metallic targets (foils) to create an approximate monochromatic source from the fluorescent photons created in the foil. Since fluorescence photons have well defined energies (i.e. are monochromatic), they provide a good source for energy calibration. In this thesis I worked as a part of the MARS "foil group" towards the aim of improving the original XRF method by Panta. The motivation for this is that the current energy calibration used by MARS is a correction per-chip (not per-pixel) which results in a 5-7 % (2-5 keV) variation in the calibration of individual pixels [2]. The primary difference between the modified XRF method investigated here and Panta's method is to measure the XRF found outside of the primary x-ray beam. This modification aims to increase the ratio of fluorescence photons to background photons remaining from the polychromatic x-ray beam. Initial testing of the method, however, did not consistently detect the fluorescence for the various metal foils of interest, this led into an investigation for optimising the thickness of the foils used to ensure that maximum fluorescence is escaping the foil.

The outcome of the initial foil experiments lead to the development of a model for determining the optimal thickness that each foil should be in order to obtain a maximum

fluorescence signal. Two stages of the model were developed: (1) the simple model for determining optimal foil thickness that assumes a monochromatic beam and calculates the optimum foil thickness at specific energies; and (2) the energy integrating model is a polychromatic model that uses numerical integration across all energies to give the foil thickness at which a maximum fluorescence signal is detected. These models are based purely on underlying physical principles and show promising results. The models confirm that the initial testing used sub-optimal foil thicknesses, explaining the low fluorescence signal in the initial experiments of the modified XRF method. The optimal foil thickness model is being used to plan the next stage of experiments that the foil group will perform.

The energy calibration of the MARS multi-energy scanner is carried out prior to scanning and can be used as a quality control tool. An accurate energy calibration technique enables better image reconstruction by improving the energy resolution of the system. The image contrast is also improved allowing for more accurate material characterisation. In this thesis some of the short-comings of the previous energy calibration technique are overcome by the development of a theoretical model. A more accurate energy calibration allows for a more accurate material analysis which is the foundation for all applications using MARS. When the XRF technique has been fully optimised it will be automated and integrated into the MARS system.

My contribution in the MARS project is highlighted in the previous paragraphs and in section 1.4. This chapter provides a brief overview of multi-energy CT and MARS in section 1.1. The motivation for developing the theoretical model for optimum foil thickness is discussed and some desired improvements to the MARS image reconstruction are mentioned. The clinical significance of this work is given in section 1.2, and finally an outline of the remaining chapters of this thesis will be given in section 1.3.

1.1 Overview

An x-ray beam consists of a stream of high energy photons. Each of these photons have a specific energy. Computed tomography (CT) is an imaging modality which produces 3D images of the inside of objects using x-rays. CT scanners use polychromatic x-ray sources which emit x-rays of varying energies. When an x-ray beam passes through an object the photons are attenuated to different degrees depending on the atomic composition of the material it is passing through and the energy of the respective photons. CT uses the attenuation of x-rays to reconstruct the internal structure of an object. Conventional CT measures x-rays using energy integrating detectors, and therefore cannot discriminate the energy dependent characteristics of x-ray attenuation. Multi-energy CT scanners

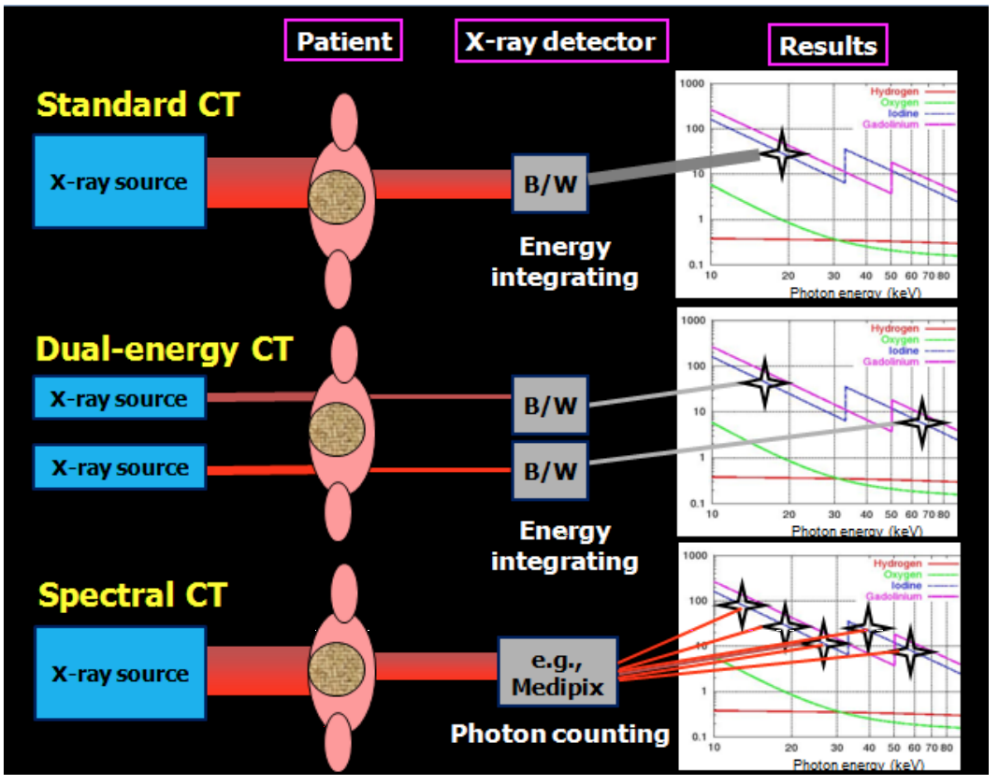

FIGURE 1.1: Illustration of differences between conventional CT (top), dual-energy CT (middle) and MARS multi-energy (spectral) CT (bottom). Conventional CT measures attenuation over the entire broad spectrum, dual-energy detects two attenuated spectra and the MARS multi-energy scanner detects the attenuated signal at different energies by using Medipix technology. Image retrieved from Anderson et. al. (2010) [6].

measure the absorption of x-rays in different energy ranges. Using the differences in x-ray absorption in these energy ranges it is possible to discriminate between, and quantify, various materials in an object [3].

The first attempts to exploit the energy dependence of x-ray photons was done with dual-energy CT by Alvarez and Macovski in 1976 who used it to split a dual energy signal into its photoelectric effect and Compton scattering contributions [4]. Dual energy CT is typically done using either the dual-source or kVp switching method. Fast kVp switching is a fairly new development which rapidly switches the x-ray tube voltage between two levels for alternate projection views [5]. However, the slower image acquisition time needed for kVp switching and the multiple x-ray sources in dual source result in an increased dose to the patient for dual energy CT compared to conventional CT. Figure 1.1 shows the evolution of CT imaging from conventional CT to multi-energy (spectral) CT.

MARS is a multi-energy (spectral) computed tomography (CT) scanner which uses the Medipix range of energy-discriminating photon-counting detectors. A picture of the

FIGURE 1.2: A picture of the MARS scanner in a lab at the University of Canterbury.

MARS scanner is shown in Figure 1.2. The latest MARS scanners use the Medipix3RX detectors, which use advanced inter-pixel communication known as charge summing [7] to significantly reduce cross-talk between detector pixels. The MARS scanner separates a polychromatic x-ray spectrum into energy bins to extract energy information from the x-ray beam as shown in Figure 1.1. The Medipix detector chips can discriminate whether to count the x-ray photons in each energy bin by comparing their incident photon energy to an energy threshold on the detector chip. If the energy of the photon is above the threshold then it is counted. The current Medipix chip (Medipix3RX) can compare each photon measurement to 8 different energy thresholds, and has a pixel size of 110 $\times$ 110 μm [8].

Currently MARS is only available as a small animal scanner which is suitable for scanning small animal models and excised samples of human and animal tissue. The MARS research team includes physicists, medical physicists, mathematicians, engineers, computer scientists, biologists, surgeons, and clinical radiologists. Over the next five years the MARS team will be up-scaling this technology to produce a human scale MARS scanner that is suitable for clinical use.

Multi-energy CT scanners which use energy-discriminating photon-counting detectors such as Medipix3RX offer significantly higher energy resolution than the common clinical

dual-energy scanner. For image reconstruction and material analysis to take advantage of all the energy information offered by MARS, the detector's energy response must be well understood and calibrated accurately. Improving the image reconstruction algorithm used for the MARS scanner has been a topic of ongoing research and development for the MARS team. In 2014 an internal document titled "Using Beer's law in MARS scanner" was distributed by Butler *et. al.* [9] to facilitate discussion on how to improve the MARS spectral CT image reconstruction algorithm. The current reconstruction algorithm consists of a monochromatic model being applied to a polychromatic beam, which is the common approximation made in conventional and dual-energy CT. However, to move to a polychromatic reconstruction algorithm, it was identified that more accurate energy calibration would be essential. This provided the motivation for developing the improved per-pixel XRF energy calibration method presented in this thesis.

1.2 Clinical significance

MARS is advantageous compared to conventional and dual-energy CT and is a significant improvement in medical imaging technology. MARS offers simultaneous discrimination of soft tissues, bone, and multiple contrast pharmaceuticals.

Some studies exploiting the advantages of the MARS multi-energy scanner include: (1) distinguishing fat from liver material for improving the non-invasive diagnosis of Non-Alcoholic Fatty Liver Disease (NAFLD) [10]; (2) locating and quantifying tumours in mice by the injection of gold contrast [11]; and (3) the identification and grading of osteoarthritic cartilage [12]. The work in this thesis has the potential to contribute significant advances in imaging with MARS by enhancing the energy resolution obtained from the Medipix detectors and improving the sensitivity and specificity of tissue characterisation.

1.3 Thesis outline

This thesis reports on developments made in the energy calibration of a multi-energy x-ray detector. An overview of the background material to this work (x-rays, x-ray interactions and image reconstruction) is presented in chapters 2 and 3. The work using the modified XRF method is covered in chapter 4. The theoretical model for optimum foil thickness is developed in chapter 5, showing both the monochromatic and the polychromatic models. Finally, a conclusion to the thesis is given in chapter 6. Detailed summaries for chapters 1-5 are provided below.

Chapter 1 provides an introduction to the background and motivation of the thesis and a brief outline of the contents of the thesis. It also has a list of publications related to this thesis.

Chapter 2 provides an overview of the x-ray interactions that are encountered in clinical x-ray imaging. This includes x-ray production, attenuation of x-rays and an overview of the Beer-Lambert law.

Chapter 3 provides an overview of multi-energy CT. This chapter covers data acquisition and gives some general information about the Medipix detectors. The image reconstruction with MARS multi-energy CT is covered and possible improvements to the current reconstruction technique are discussed.

Chapter 4 discusses the previous X-ray Fluorescence (XRF) technique used by members of the MARS team, and the modified XRF technique is an extension of the original work that aims to improve the fluorescence signal. The thickness of the foils used in the XRF technique is briefly discussed.

Chapter 5 develops a simple monochromatic model for determining the optimum foil thickness to obtain a maximum fluorescence signal. The energy integrating model then extends the optimal foil thickness model to a polychromatic beam.

Chapter 6 gives a conclusion to the thesis.

1.4 List of publications

Over the course of this thesis, and the time I spent with the MARS group in 2013, I have been a co-author on 2 published papers.

1. R. Aamir, A. Chernoglazov, C. J. Bateman, A. P. H. Butler, P. H. Butler, N. G. Anderson, S. T. Bell, R. K. Panta, J. L. Healy, J. L. Mohr, K. Rajendran, M. F. Walsh, N. de Ruiter, S. P. Gieseg, T. Woodfield, P. F. Renaud, **L. Broeke**, S. Abdul-Majid, M. Clyne, R. Glendenning, P. J. Bones, M. Billinghurst, C. Bartneck, H. Mandalika, R. Grasset, N. Schleich, N. Scott, S. J. Nik, A. Opie, T. Janmale, D. N. Tang, D. Kim, R. M. Doesburg, R. Zainon, J. P. Ronaldson, N. J. Cook, D. J. Smithies, K. Hodge, *MARS spectral molecular imaging of lamb tissue: data collection and image analysis*, Journal of Instrumentation, 2014, Volume 9, Issue 2. [13]

This paper demonstrates that lipid, water and bone can be discriminated in data collected by the Medipix3RX photon counting detector. The data used for this publication has been made available to enable other researchers to test their image reconstruction and material analysis techniques. My contribution to this publication includes preparing the MARS scanner for the lamb tissue scan.

2. A. Atharifard, S. T. Bell, M. Ramyar, B. Goulter, M. F. Walsh, **L. V. Broeke**, A. P. H. Butler, *Pixel by pixel energy calibration of MARS camera*, Proceedings of NZPEM 2014 Nov 20-21st, Christchurch, New Zealand.

   This research demonstrates that variations in energy responses of pixels of MARS camera is a limiting factor for global energy resolution and the image quality. Up to 5 keV dispersion of threshold energy across the detector array has been observed. A method that quantifies the error in energy responses of individual pixels across the spectra and corrects for it is introduced. The results are validated through x-ray fluorescence measurements. My contribution to this research includes developing methods for the per-pixel energy calibration of the MARS scanner by working as a part of the "foil group".

Chapter 2

X-ray interactions in medical imaging

This chapter provides an introduction to the production of x-rays and some of the relevant interactions they undergo with matter in the medical field. An understanding of the basic physical principles in this chapter are paramount to understanding the ideas that are developed in the later chapters of this thesis. Section 2.1 gives a historical background to x-rays and their place in medicine. The production of x-rays are described in section 2.2. Section 2.3 gives more detail regarding the atomic structure of an atom so that the interactions of photons with matter can be fully understood in section 2.4. The Beer-Lambert law is introduced in section 2.5 and the relevant x-ray interaction contributions are mentioned. The chapter concludes with a summary in section 2.6.

2.1 Overview

X-rays are a form of high energy electromagnetic radiation that were first discovered by the German physicist Conrad Wilhelm Röntgen in 1895 during his research on cathode rays. He noticed that a plate of barium platino-cyanide crystals in his lab glowed when he activated the cathode ray tube. Röntgen linked this to the working of the tube and named this strange phenomena x-rays. In next experiments he used a photographic plate to make his first x-ray images. His approach involved firing a uniform field of x-rays through an object and measuring a representation of the ionising properties of x-ray photons on the other side. X-rays are attenuated in the object and the detected x-rays reveal information about the inner structure of the object. Soon after Röntgen's

discovery x-rays started being exploited for medical purposes. They were used by surgeons to locate things like bullets and bone fractures in their patients. X-rays were also seen to have a positive effect on arthritis, skin diseases and some cancers.

Within the medical community x-rays are an important tool for imaging the interior of a human body. X-rays in the energy range 20 - 150 keV are used in medical imaging, while x-rays up to 20 MeV are used in the treatment of many cancers. One of the most commonly used diagnostic imaging modalities in hospitals is known as computed tomography (CT). CT is based on computing the 3D internal structure of an object from a sequence of 2D x-ray images.

2.2 Production of x-rays

2.2.1 The x-ray tube

In medical imaging, x-rays are nearly always created in an x-ray tube. A schematic representation of a conventional x-ray tube is shown in Figure 2.1. The x-ray tube consists of a vacuum glass envelope, at one end of which is the cathode and at the other end an anode.

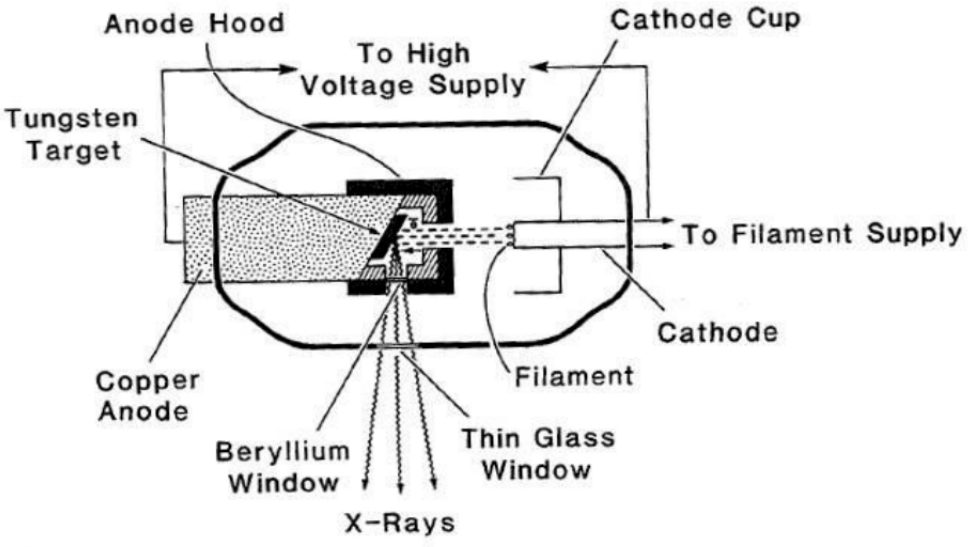

FIGURE 2.1: Schematic of x-ray tube with fixed anode. Figure retrieved from Khan 2003 [14].

When the cathode is heated, electrons are produced via thermionic emission. Emitted electrons travel towards the anode and are accelerated to a high speed due to a voltage applied between the cathode and anode. The electrons attain kinetic energies equal to the product of the electrical charge and potential difference (typically given in units

of eV). Most of the energy exchanges with electrons in the target give rise to heat. However, a small fraction of the accelerated electrons come within the proximity of an atomic nucleus and are deflected by its positive electric field, causing a conversion of some of its kinetic energy into an x-ray photon. The amount of energy lost by the electron, and thus the energy of the resulting x-ray, are determined by the distance between the electron and the nucleus of the anode target atom [15]. Electrons passing in closer proximity lose more kinetic energy and thus emit higher energy x-rays. This process is known as Bremsstrahlung and is shown in Figure 2.3 (a).

Each of the electrons are deflected at slightly different angles and so they create photons of varying energies, creating a continuous Bremsstrahlung radiation spectrum. Bremsstrahlung consists of a full spectrum of x-rays with various energies. Some higher energy Bremsstrahlung x-rays ionise the target material, while some lower energy Bremsstrahlung x-rays are absorbed (filtered) in the anode before they leave the tube. Characteristic x-rays are produced from bound electrons moving from an outer shell to vacant positions in inner shells, and will be discussed in more detail in the next section of this chapter. The Bremsstrahlung and characteristic components of an x-ray beam are shown in Figure 2.2.

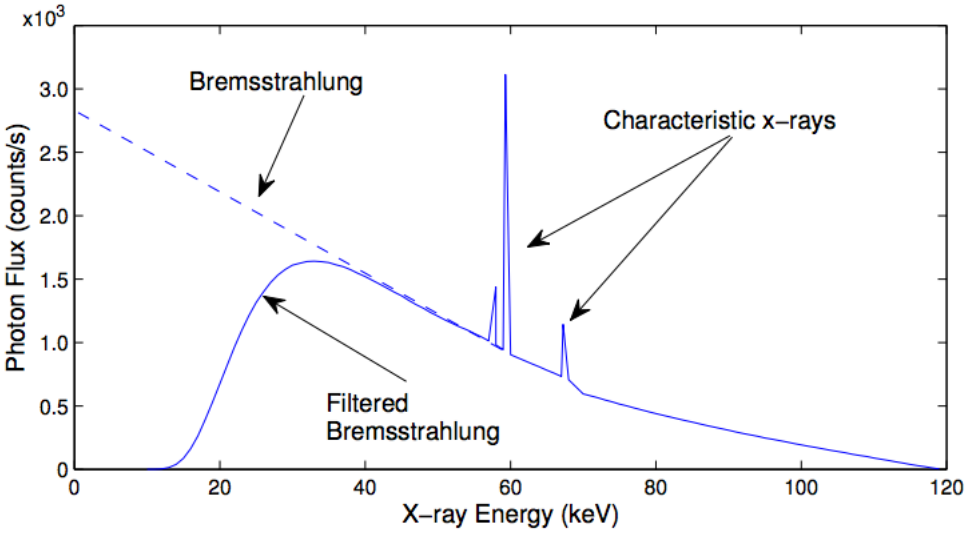

FIGURE 2.2: Example 120 kVp x-ray spectrum output from a tungsten anode x-ray tube. Bremsstrahlung and characteristic x-ray components are identified. Figure retrieved from Batheman (2014) [16].

2.2.2 Characteristic x-rays

In addition to the continuous Bremsstrahlung x-ray spectrum, discrete x-ray energy peaks called characteristic radiation may be present. Characteristic x-rays are also

known as fluorescence x-rays. Electrons in an atom are distributed in shells (see section 2.3), each of which has an electron binding energy. The electron binding energies are characteristic of an element. When the energy of an incident electron, determined by the voltage applied to the x-ray tube, exceeds the binding energy of an electron shell in a target atom, a collisional interaction can eject an electron from its shell, creating a vacancy. An outer shell electron with less binding energy immediately transitions to fill the vacancy, and a characteristic x-ray is emitted with an energy equal to the difference in the electron binding energies of the two shells. This emission gives rise to several discrete characteristic energy peaks superimposed on the Bremsstrahlung spectrum, as shown in Figure 2.2. The energies of the fluorescence photons are unique to the anode material and have a monochromatic energy. The process of creating a characteristic x-ray is shown in Figure 2.3 (b).

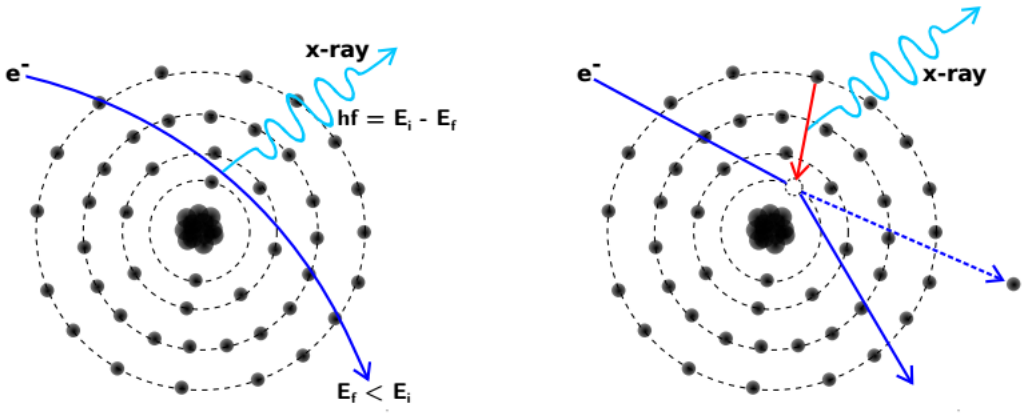

(a) Bremsstrahlung (b) Characteristic X-rays

FIGURE 2.3: (a) When an electron is decelerated in an atom's electric field the electron's trajectory is changed slightly. The change in kinetic energy of the electron is emitted in the form of an x-ray photon. The full spectrum of emitted x-rays is known as Bremsstrahlung radiation. (b) Characteristic (fluorescence) x-rays have discrete energies and are the result of a bound inner shell electron being emitted from the atom by an incoming (free) higher energy electron. An electron from an upper atomic shell drops down to fill this vacancy, emitting a characteristic x-ray photon in the process. The energy of the photon is the difference in binding energy of the two electron states. Image retrieved from Bateman (2014) [16]

2.3 Orbital shells and sub-shells

An atom is comprised of orbital shells (K, L, M, N,..). These letters are associated with the principal quantum numbers n = 1, 2, 3, 4,.... The innermost shell is designated the K-shell and has the highest electron binding energy, followed by the L, M and N shells,

with progressively lower binding energies. Each shell of an atom is subdivided into sub-shells which are made up of orbitals (s, p, d and f). No two orbitals have the same energy level. When there are multiple electrons in an atom they interact and split the orbitals into slightly different energies. The fine splitting between orbitals result in two distinct peaks. This comes from the spin-orbit interaction energy (i.e. spin-orbit coupling) between the electron spin and the orbital momentum. The conventional symbols used to represent the characteristic x-ray lines of the K and L series, and the associated atomic shells and sub-shells, are shown in Figure 2.4. The fluorescence photons arise from discrete transitions between these shells, therefore the fluorescence photon will be monochromatic.

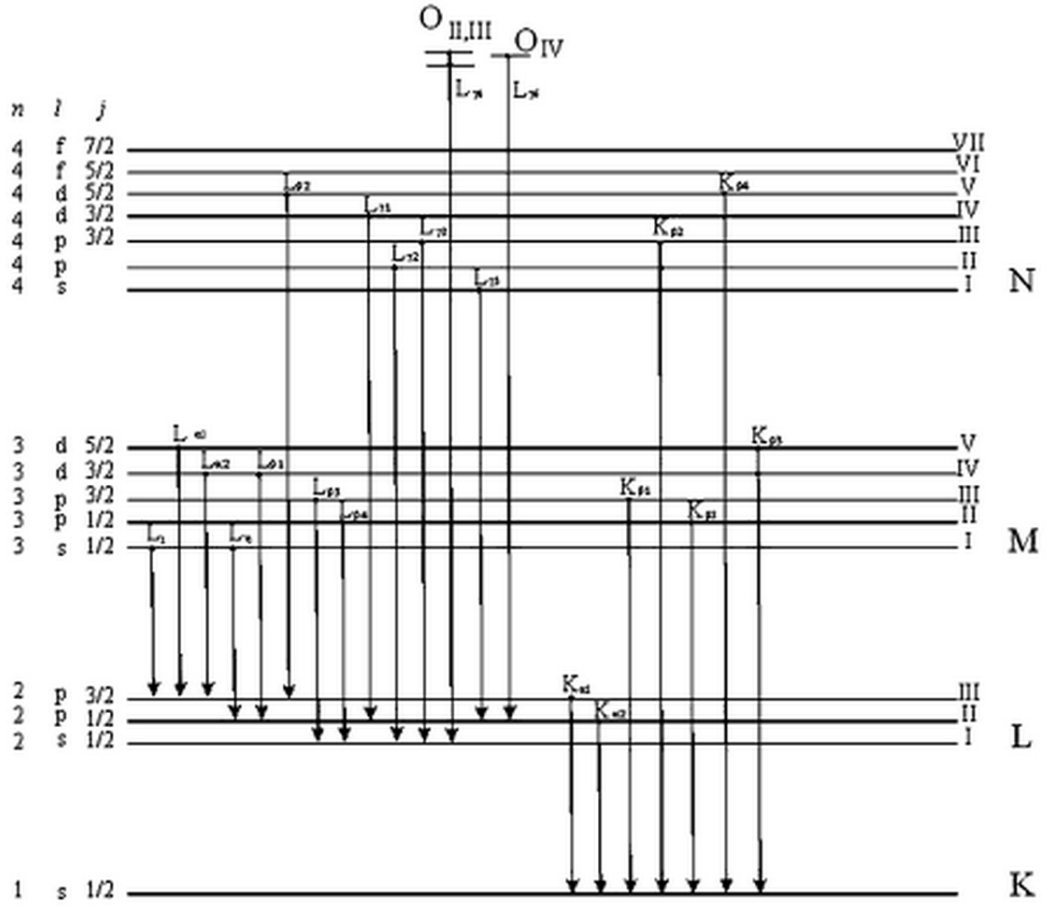

FIGURE 2.4: The K and L series of characteristic x-ray lines. Figure retrieved from Cierniak (2011) [17].

2.4 Naming of characteristic x-rays and fluorescence

Fluorescence photons are named according to the orbital in which the vacancy occurred. For example, the radiation resulting from a vacancy in the K shell is called

a K-fluorescence x-ray. If the vacancy in one shell is filled by the adjacent shell, it is defined by a subscript α (e.g., L $\rightarrow$ K transition= K_α). If the electron vacancy is filled from a non-adjacent shell, the subscript β is used (e.g., M $\rightarrow$ K transition= K_β). The additional subscripts 1 and 2 are used for the two distinct peaks that form due to spin-orbit coupling [*]. The energy of the fluorescence photon is the difference between the electron binding energies of the respective shells. The energies of various K-shell fluorescence photons for a tungsten anode target are shown in Table 2.1.

Shell transition	Tungsten (keV)
$K_{\alpha 1}$	59.32
$K_{\alpha 2}$	57.98
$K_{\beta 1}$	67.24

TABLE 2.1: The energies of various K-shell fluorescence photons for a tungsten anode target

Although the concepts in the previous paragraphs are applied to the anode material specifically, an understanding of the atomic structure and naming of atomic orbitals is essential in the development of the model used for determining optimum foil thickness (chapter 5) which considers how to obtain maximum K-shell fluorescence emitted from various metal foils.

2.5 Interaction of x-rays with matter

When x-rays pass through matter they can be attenuated through one of four major types of interactions, three which are relevant to this research and play a role in diagnostic radiology: (1) Rayleigh scattering; (2) Compton scattering; and (3) photoelectric absorption (Figure 2.5), and the other being pair-production (which will not be covered here as it requires energies above 1 MeV).

Rayleigh scattering

In Rayleigh scattering the incident photon interacts with and excites the total atom, as opposed to the individual electrons as in Compton scattering or the photoelectric effect. This interaction occurs mainly with very low energy x-rays. During the Rayleigh scattering event, the electric field of the photon's electromagnetic wave expends energy, causing all of the electrons in the scattering atom to oscillate in phase. The atom's electron cloud immediately radiates this energy, emitting a photon of the same energy but in a slightly different direction, as shown in Figure 2.5. The angle of the scattering is usually low in the forward direction. However, the probability of occurrence of this interaction in the diagnostic energy range is low.

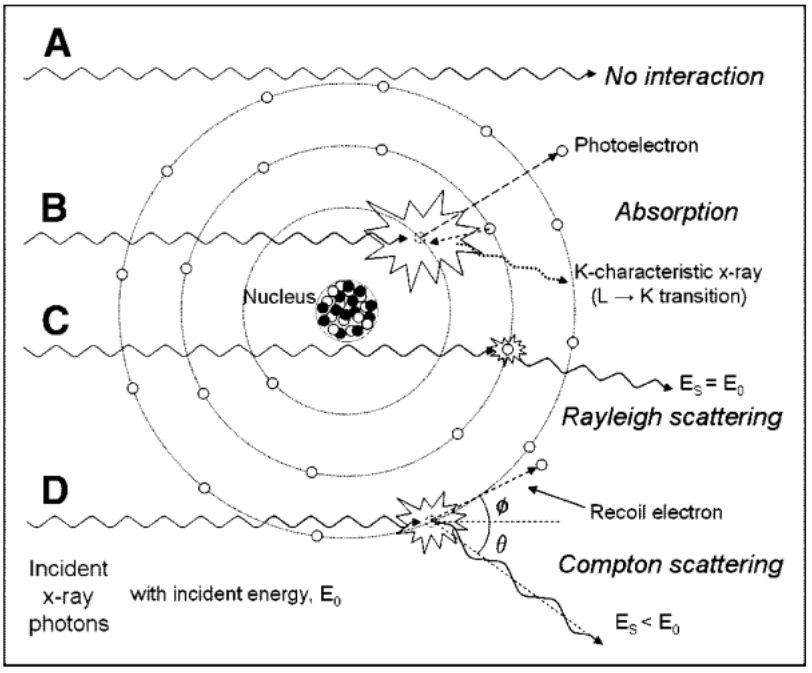

FIGURE 2.5: Different interactions x-rays can have with matter: B) photoelectric absorption, C) Rayleigh scattering, and D) Compton scattering. Image retrieved from Seibert and Boone (2005)[18].

Compton scattering

Compton scattering is the predominant interaction of x-ray photons in the diagnostic energy range with soft tissue. This interaction is most likely to occur between photons and outer-shell electrons. The electron is ejected from the atom, and the scattered photon is emitted with some reduction in energy relative to the incident photon (both energy and momentum are conserved), as shown in Figure 2.5. Thus, the energy of the incident photon is equal to the sum of the energy of the scattered photon and the kinetic energy of the ejected electron. The direction of the scattered photon is based on the direction of the ejected electron. Compton scattering is most likely to occur in the outer-shell electrons, with no subsequent movement of electrons and ejection of characteristic x-rays. The probability of a Compton scattering interaction increases when the photon energy is higher.

Photoelectric absorption

Photoelectric absorption is the liberation of an electron from an atom through complete absorption of an x-ray. An electron ejected through the photoelectric effect is called a photo-electron. The kinetic energy of the ejected photo-electron, E_{pe}, is equal to the incident photon energy, E_0, minus the binding energy of the orbital electron, E_b.

$$E_{pe} = E_0 - E_b \tag{2.1}$$

The vacancy left by a photo-electron enables the production of a characteristic x-ray as described in section 2.2.

In order for the photoelectric effect to occur, the incident photon energy must be greater than or equal to the binding energy of the electron that is ejected. The likelihood of a photoelectric interaction occurring is highest when the binding energy is just below the incident photon energy. For example, for photons whose energies exceed the K-shell binding energy, photoelectric interactions with K-shell electrons are most probable. Following a photoelectric interaction the atom is ionised with an inner shell electron vacancy. This vacancy will be filled by an electron from a shell with a lower binding energy. This creates another vacancy, which, in turn is filled by an electron from an even lower binding energy shell. Thus, an electron cascade from outer to inner shell occurs. The difference in binding energy is released as either characteristic x-rays (fluorescence) or Auger electrons.

The probability of a fluorescence photon emission decreases as the atomic number of the absorbed decreases. At low energies there is a large divergence in the attenuation for different materials, creating the opportunity to differentiate materials in energy ranges that are strongly controlled by the photoelectric absorption (Compton scattering does not vary much between materials). The idea of the photoelectric absorption probability is discussed in more detail in chapter 5.

As mentioned above, a photon cannot undergo a photoelectric interaction with an electron in a particular atomic shell or sub-shell if the photon's energy is less than the binding energy of the shell or sub-shell. This causes the dramatic decrease in the probability of photoelectric absorption for photons whose energies are just below the binding energy of a shell. Thus, the photon energy corresponding to an absorption edge is the binding energy of the electrons in that particular shell or sub-shell. This phenomenon is exploited in K-edge imaging which uses the fact of the K-edge to help identify contrast pharmaceuticals containing elements such as iodine and barium [19]. An absorption edge is designated by a letter representing the atomic shell of the electrons, followed by a roman numeral subscript denoted the sub-shell (e.g. K, L_I, L_{II}, L_{III}).

2.6 Beer-Lambert law

X-rays are attenuated through various interactions when they pass through an object, resulting in a reduction in the beam intensity (flux). If an object is made up of multiple materials the x-ray beam will be attenuated by different amounts as it passes through

the material, which enables medically useful images to be acquired through x-ray imaging. The intensity of an x-ray beam passing through a homogeneous body of material decreases exponentially with distance and can be represented by the Beer-Lambert law (also known as Beer's law):

$$I(E) = I_0(E)e^{-\mu(E)x} \tag{2.2}$$

where $I_0(E)$ is the initial x-ray beam intensity, $\mu(E)$ is the linear attenuation coefficient and x is some distance through the object. The probability that an x-ray will be attenuated as it passes through the object is given by the exponential in the Beer-Lambert law (transmission fraction).

The monochromatic Beer-Lambert law can be extended for polychromatic x-ray beams by integrating the monochromatic Beer-Lambert law over all energies (with E_{max} being the maximum energy), giving

$$\int_0^{E_{max}} I(E)dE = \int_0^{E_{max}} I_0(E)exp\left(-\sum_v \mu_v(E)l_v x\right)dE \tag{2.3}$$

The limits of the integration of Equation 2.3 creates an energy dependence for all energies ranging from 0 to the x-ray tube voltage (defined by the kVp).

2.6.1 X-ray interaction contributions

The x-ray interactions mentioned in section 2.4 are important for material analysis in multi-energy x-ray imaging as they characterise which materials the x-ray beam has passed through. This is highlighted by Alvarez and Macovski's 1976 paper [3] which shows that dual-energy CT projection images can be broken up into their photoelectric and Compton contributions. The linear attenuation coefficient (units cm^{-1}) introduced in Equation 2.2 is made up of contributions from each type of photon interaction: photoelectric absorption (τ); Rayleigh and Compton scattering (σ_R and σ_C).

$$\mu = \tau + \sigma_R + \sigma_C \tag{2.4}$$

The linear attenuation component for photoelectric absorption (Equation 2.5), Rayleigh scattering (Equation 2.6) and Compton scattering (Equation 2.7) interactions depend on the atomic number Z and the x-ray beam energy E:

$$\tau \propto \frac{Z^n}{E^3} \tag{2.5}$$

$$\sigma_R \propto \frac{Z^2}{E^2} \tag{2.6}$$

$$\sigma_C \propto Z f_{KN}(E) \tag{2.7}$$

where the coefficient n for the photoelectric contribution varies between 4 and 5 over the energy range of interest, and $f_{KN}(E)$ is the Klein-Nishina function [*].

In general, the photoelectric effect dominates at low energies. As the energy increases the photoelectric effect and Rayleigh scattering decrease faster than the Compton effect and eventually they dominate (above the diagnostic imaging range). As Z increases the overall pattern of the energy dependence does not change.

2.6.2 Mass attenuation coefficient

The linear attenuation coefficient of a material $\mu(E)$ is directly proportional to the density, ρ, of that material. When a narrow beam of monochromatic photons with an incident intensity I_0 penetrate a layer of material of thickness, x, and density, ρ, the Beer-Lambert law (Equation 2.2) can be modified to

$$I = I_0(E) e^{-\left(\frac{\mu}{\rho}\right)(E)x} \tag{2.8}$$

where $\left(\frac{\mu}{\rho}\right)(E)$ is the mass attenuation coefficient (units $\mathrm{cm}^2\ \mathrm{g}^{-1}$). The mass attenuation coefficient is often used as a measure of a material's attenuation because it is independent of the amount (or mass) of the material. The mass attenuation coefficient is made up of contributions from the different types of photon interactions. The size of each interaction's contribution is different for x-rays of different energies, as shown in Figure 2.6.

2.7 Summary

- X-rays produced by cathode ray discharge tubes (x-ray tubes) contain a combination of Bremsstrahlung and characteristic x-ray radiation.
- Photoelectric absorption, Rayleigh and Compton scattering are the three types of x-ray interactions that occur within the diagnostic imaging range.
- The Beer-Lambert law describes the reduction in x-ray beam intensity as the beam passes through an object.

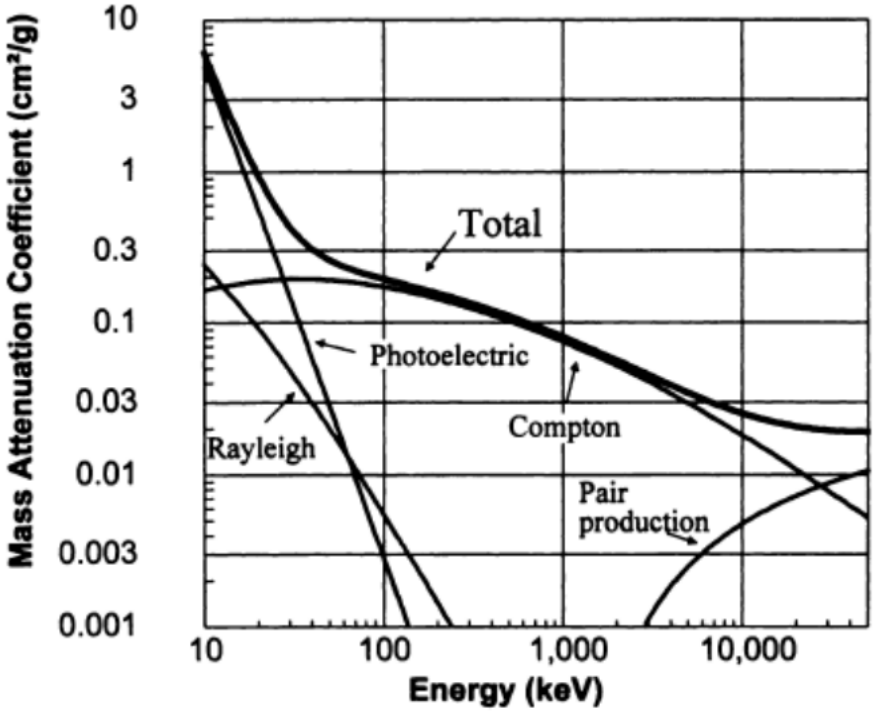

FIGURE 2.6: The attenuation coefficient is made up of contributions from many different types of photon interaction. The size of each interaction's contribution is different for x-rays of different energies. Image retrieved from Bushberg et al. (2001) [15].

- The linear attenuation coefficient is the proportionality coefficient of the differential form of the Beer-Lambert law. This coefficient can be represented as either the sum of cross-sections for each type of x-ray interaction, or as the combination of linear attenuation coefficients for the materials constituents.

- The mass attenuation coefficient is independent of the amount of material present. It is obtained by dividing the linear attenuation coefficient by the density of the respective material.

Chapter 3

MARS multi-energy CT energy calibration

In this chapter an overview of the image reconstruction with MARS multi-energy CT is given. Multi-energy CT is often referred to as spectral CT. However, dual-energy CT will refer specifically to dual energy modalities, and multi-energy will refer to both dual-energy CT and modalities of CT capable of measuring more than two energy ranges such as the MARS scanner. Energy calibration measures the energy response of the pixels in the detector and ensures that the images taken with the MARS scanner are physically accurate.

Section 3.1 gives an overview of multi-energy CT. The data acquisition is covered in section 3.2. Section 3.3 talks about the Medipix photon-counting energy-discriminating x-ray detector (PCXD) that is used in MARS imaging and it also specifically covers the operation and some of the limitations of the Medipix3RX version. Section 3.4 mentions the reconstruction techniques used in MARS multi-energy CT, and the chapter is summarised in section 3.5.

3.1 Overview

As noted previously, the potential for x-ray imaging was discovered by Wilhelm Röntgen in 1895. Since then, x-rays have formed an important medical tool for imaging the interior of a human body. X-ray imaging is based on the simple principle that a known amount of x-rays travel from an x-ray source towards the object and the object attenuates the x-rays, reducing the amount of x-rays that are detected behind the object. The degree of x-ray attenuation inside the object gives information about the object's inner

structure in the form of 2D radiographic projection images. A limitation of only having a 2D projection is that the different materials along the path of the x-ray beam overlap in the image and so distinguishing them is challenging. This limitation was overcome by the introduction of CT in the 1970's. CT is able to produce 3D radiographic images that represent a distribution of x-ray attenuation, allowing different materials (like tissue and bone) to be distinguished.

In a CT scan multiple x-ray images of an object are taken from different orientations. The 3D images are reconstructed from the projections of an object taken at different orientations (Figure 3.1). The mathematical principles behind such image reconstruction were established by Johann Radon in 1917 [1]. Reconstruction techniques have grown in sophistication but are still based on Radon's work.

The first CT scanner, developed by Sir Godfrey Hounsfield, was introduced into medical practise on 1st October 1971 at Atkinson Morley's Hospital, in London, England with a successful scan on a lady with a suspected frontal lobe tumour. The scanner produced an image with an 80×80 matrix, taking about 5 minutes for each scan, with a similar time required to process the image data [20, 21]. In 1975 Hounsfield built a whole-body scanner. The success of this was a major driving force behind the development of multi-energy variants of CT. In the last ten years the use of energy-discriminating photon-counting detectors for multi-energy CT have been investigated. Energy-discriminating photon-counting detectors assign photons to different bins based on their energy [22] (discussed in more detail in section 3.3.).

Multi-energy CT is an emerging technology which is capable of resolving the energy components of an incident x-ray beam, hence it can be used to determine properties of the materials it is passing through by a technique known as basis (or material) decomposition. The decomposition of a multi-energy CT projections into their photoelectric and Compton scattering components was first demonstrated by Alvarez and Mocovski in 1976 [23].

3.2 Data acquisition in multi-energy CT

In conventional and in multi-energy CT projection images of the object are taken from various positions as the gantry rotates. The object, placed in the middle of the gantry, attenuates the x-ray emitted from the source. The relationship between the emitted and measured x-ray beam intensity is given by the Beer-Lambert law (Equation 2.8). The relative position of the x-ray source, detector array and rotating gantry is shown in Figure 3.1.

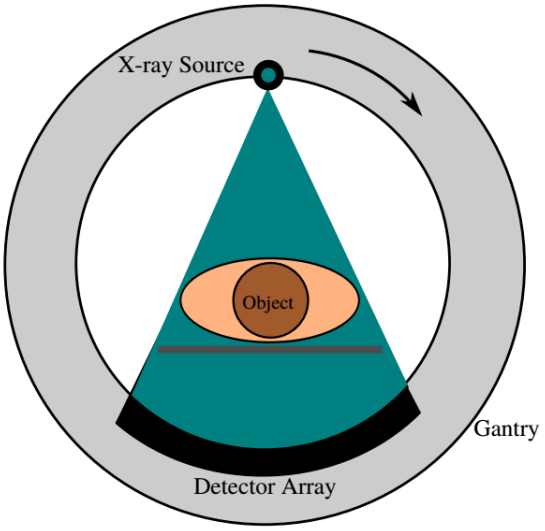

FIGURE 3.1: Relative position of the x-ray source, object and detector array in a CT scanner. 2D projection images are used to construct 3D images of the object. Image retrieved from Bateman (2014) [16].

Detector technology has passed through various improvements since the discovery of x-rays in 1895. Detection systems are categorised by the way they interact with x-rays (direct and indirect). Conventional clinical CT systems use scintillator detectors that operate in energy-integrating mode. Photon counting detectors use a pulse height discriminator that separates signal pulses from the noise pulses, enabling high-precision measurement. A comparison between integrating devices and photon counting detectors, as summarised by Jakubek (2007) [24], is given below.

Integrating devices	Photon counting pixel detectors (Medipix)
High spatial resolution	Good spatial resolution
Zero dead time	Non zero dead time
Not energy sensitive	Energy discrimination
Noise	No noise

3.3 Energy-discriminating photon-counting detectors

The advantages of photon counting x-ray detectors (PCXDs) with energy discrimination capabilities are considered to be influential in multi-energy CT. The energy-discriminating features are based on the pulse height analysis of an incident x-ray and assigns the x-ray to one of several energy bins. The number of energy windows per detector pixel in PCXDs varies from 2 to 8, depending on specific detector designs [25]. Commonly known advantages of the PCXDs include a significantly higher contrast to

noise ratio (CNR) and a reduction of radiation dose [26]. Another advantage of PCXDs is that they are highly sensitive to low-energy x-rays, whereas charge-integrating detectors are more sensitive to higher energy x-rays [27]. An example of energy-discriminating PCXDs include the Medipix series of detectors, which will be discussed in more detail later on in this section. Currently there are no commercial human imaging systems that use PCXDs.

3.3.1 The Medipix detector

The Medipix detector, developed by an international collaboration hosted by the European Organisation for Nuclear Research (CERN), is the energy-discriminating PCXD used in MARS multi-energy CT. The Medipix detector counts every incident photon. It's small pixel size gives a high contrast between different materials along with high spatial resolution [28]. The Medipix detector offers substantially more information regarding the object being imaged.

Three generations of the Medipix chips have been successfully developed. The first model of the Medipix detector (Medipix1) was released in 1991 and had 64 $\times$ 64 pixels, each having dimensions of 170$\times$170 μm^2 [29]. Each pixel in the Medipix1 contained a single energy threshold that could be set and energies below this threshold were not counted. The improvements made for the Medipix2 detector allowed for a 256$\times$256 detector array, each pixel with dimensions of 55$\times$55 μm^2. The Medipix2 had two thresholds per pixel so it could count photons within a specified energy window [30] giving it higher energy resolution than the Medipix1. The Medpix3 has multiple energy counters and could measure eight different energy ranges per exposure when used in a mode with 110$\times$110 μm^2. The Medipix3 PCXD had two operational modes: (1) single pixel mode; and (2) charge summing mode (CSM) [31]. CSM uses inter-pixel communication to solve issues of cross-talk (charge-sharing) between pixels. Some of the deficiencies of inter-pixel communication in Medipix3 were solved with the Medipix3.2 (also known as the Medipix3RX) [32].

The Medipix detectors are hybrid detectors consisting of a semiconductor sensor layer (such as Si, GaAs, CdTe, or CdZnTe) that is solder-bump bonded (or otherwise connected) to a Complementary Metal-Oxide-Semiconductor (CMOS) Application Specific Integrated Circuit (ASIC) readout layer. A schematic representation of the Medipix detector is shown in Figure 3.2.

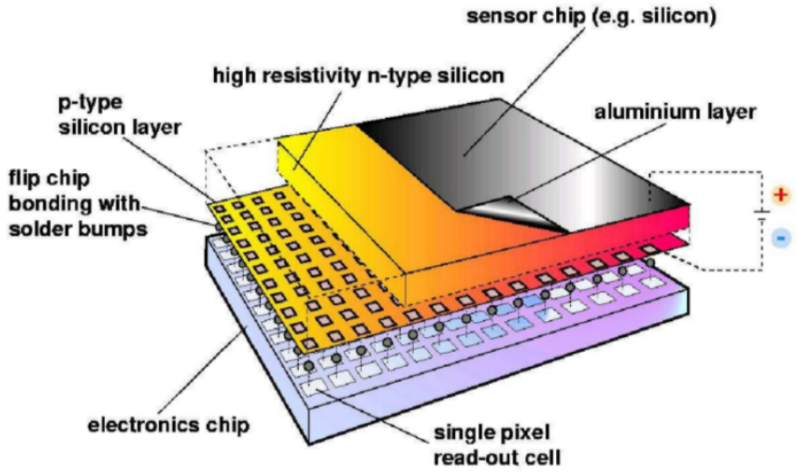

FIGURE 3.2: Schematic of a Medipix detector. Image retrieved from Zainon (2012) [33].

3.3.2 Operation of the Medipix3RX

Each pixel in the Medipix3RX contains an analogue section, followed by a digital section [34]. The analogue section determines the global energy threshold using a digital-to-analogue converter (DAC). The global energy threshold is set via a reference current and refers to ASIC parameters that are controlled by a single DAC applied to all pixels. When photons strike the detector, electron-hole pairs are created within a tiny volume in the sensor layer. The separation of the electrons and holes produces a voltage pulse. The discriminator (in the analogue section of the pixel) compares the height of the pulse to thresholds selected by the user. The threshold DAC selects the range of photon energies that will be counted. If the pulse height of the charge is higher than the reference current set by the energy threshold DAC, the counter in the digital section of the corresponding pixel is incremented. Small variations in the electrical performance of the threshold discriminator affects the performance of energy-discriminating photon-counting detectors by degrading the energy resolution.

3.3.3 Energy calibration of the Medipix detector

To ensure that the images taken with the MARS scanner are clinically accurate the system must be calibrated. Energy calibration aims to measure the energy response of the pixels in the detector. The current calibration for the Medipix detector in the MARS scanner is a global energy calibration using the kVp method [1]. This technique uses the x-ray tube voltage (kVp) as a reference energy, which is stepped through an energy range of interest. The energy threshold where a pixel transitions from not-counting (off)

to counting (on) is located. A global calibration measures the average energy response across the entire pixel matrix. However, a per-pixel energy calibration is more desirable as it measures the energy response of each individual pixel [1].

The Medipix3RX detector has a 128×128 pixel array. The energy threshold across the detector is not consistent (threshold dispersion) [35], resulting in different effective threshold voltages of the analog discriminator. The Medipix3RX has 9-bit energy threshold DACs which set the same energy threshold values for all pixels in the detector. In addition, each of the two discriminators in a pixel contains an independent 5-bit fine adjustment DAC to correct for inter-pixel threshold dispersion. Optimising the fine adjustment DAC of each pixel to reduce the inter-pixel threshold dispersion is knows as threshold equalisation. However, the threshold dispersion cannot be completely eliminated by the threshold equalisation procedure due to the limited range and resolution of the fine adjustment DAC [34]. The inter-pixel variation of the energy response can be a limiting factor in global spectral resolution and the precision of energy calibration [36].

3.3.4 Pulse pile-up and charge sharing

Pulse pile-up and charge sharing effects seriously limit the energy resolution of PCXDs. Pulse pile-up occurs when the time interval between two consecutive photon events in the PCXDs is so small that the successive pulses are combined into a single photon pulse [25]. This greatly affects the energy resolution and count rate of the detector [28]. Charge sharing occurs when the three-dimensional charge cloud in the detector (created by the electron-hole pairs) is collected across several adjacent pixels. Charge sharing distorts the energy spectrum measured by a single pixel, and when unaccounted for, it appears as several lower energy photon interactions in adjacent pixels [37]. The Charge Summing Mode in Medipix3RX ASIC is an advanced mode of operation that is designed to account for the charge sharing effect in PCXDs [31].

3.4 Image reconstruction

Image reconstruction in CT is a mathematical process that generates images from x-ray projection data acquired at many angles around an object. Conventional CT reconstruction involves calculating the object's linear attenuation coefficient distribution $\mu(x, y)$ from a set of radiographic projections $p(r, \theta)$. In clinical CT the reconstruction techniques used are commonly based on filtered back projections and on the monochromatic

Beer-Lambert law:

$$p(r,\theta) = -ln(I/I_0) = \int_{T(s)} \mu(x,y)ds \tag{3.1}$$

where I is the beam intensity, I_0 is the initial intensity of the beam, $T(s)$ is some ray path at a distance r and rotation angle θ. However, since CT scanners use polychromatic x-ray sources, this approximation results in energy dependent image distortions known as beam hardening artifacts.

Two major categories of CT reconstruction methods exist, analytical reconstruction and iterative reconstruction. A type of analytical reconstruction employs the filtered back projection (FBP) method. This involves inverting the monochromatic Beer-Lambert law (Equation 3.1) using Fourier transforms and back-projecting the image along the lines they were taken from. The algebraic reconstruction technique (ART) is an iterative technique, originally developed by Kaczmarz in 1936 [38], that is capable of producing better reconstructions than filtered back projections [39].

When ART is used for CT image reconstruction it is solving a system of linear equations $A\mathbf{x} = b$ constructed from the discrete version of the monochromatic Beer-Lambert law.

$$p(r,\theta) \approx \sum_v \mu_v l_v \tag{3.2}$$

where v is the voxel index and l_v is the path length of the projection passing through voxel v.

3.4.1 Reconstruction artifacts

Reconstruction artifacts are commonly encountered in clinical CT and may give errors and distortions in the imaged object, resulting in false interpretations. Commonly encountered artifacts in CT include ring, shading, cupping, and streak artifacts [40]. Ring artifacts are caused by a mis-calibrated detector which results in rings centred on the centre of rotation. Object motion will also result in shading and streak artifacts. Beam hardening effects are visible in the form of cupping, shading and streak artifacts. Beam hardening occurs because the average energy of a transmitted spectrum increases while passing through an object [41]. Beam hardening artifacts in CT are common when using reconstruction techniques based on the monochromatic Beer-Lambert law. It has been shown that reconstruction techniques based on polychromatic models can eliminate beam hardening artifacts almost entirely [42, 43].

3.4.2 Polychromatic reconstruction

To reconstruct without beam hardening artifacts each ray needs to be modelled by the polychromatic Beer-Lambert law. The sum in Equation 3.2 is monochromatic, however, we want to extend ART to multi-energy systems (polychromatic reconstruction) so that each energy range is reconstructed separately. For a single ray the polychromatic Beer-Lambert law is given by:

$$\int_{Th}^{E_{max}} I(E)dE = \int_{Th}^{E_{max}} I_0(E)exp\left(-\sum_v \mu_v(E)l_v\right)dE \tag{3.3}$$

where E_{max} is the tube kVp.

The integral limits of Equation 3.3 are defined by the energy calibration of the detector. The DAC step chosen for each pixel must result in each pixel's threshold (Th) being at approximately the same keV, as shown in Figure 3.3. When using this description for each ray the reconstruction problem becomes a non-linear optimisation problem, sometimes referred to as joint-DE or material reconstruction [44]. The methods to solve these problems are typically iterative techniques similar to ART. A per-pixel energy calibration is preferred to a global energy calibration as the limits of the integral in Equation 3.3, Th and E_{max}, are set per-pixel.

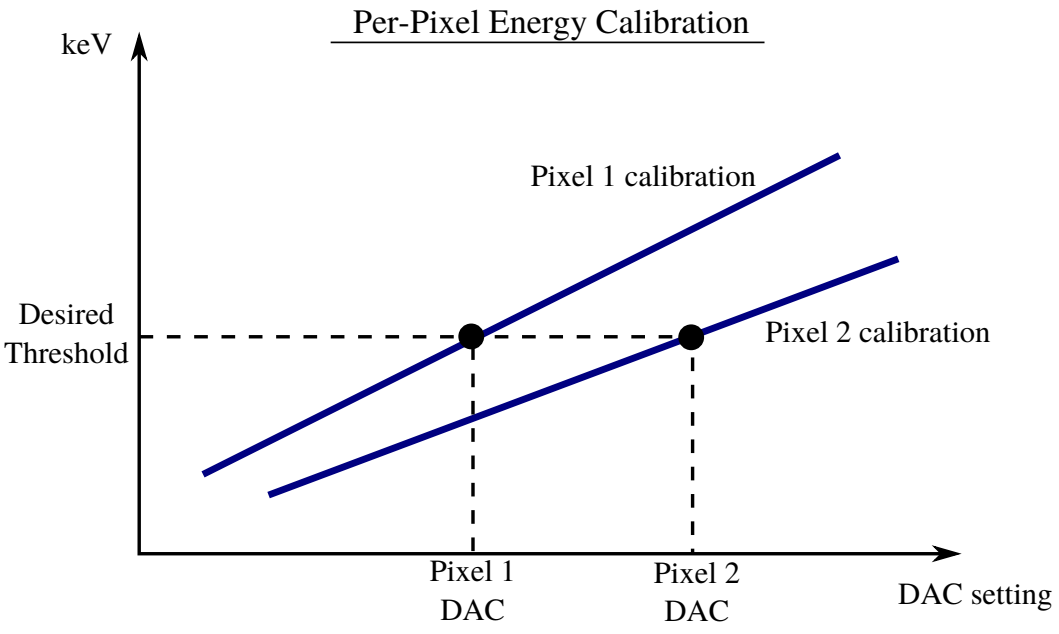

FIGURE 3.3: Plot showing how the DAC step chosen for each pixel is related to the keV in a per-pixel energy calibration.

The current image reconstruction in MARS CT approximates a polychromatic x-ray beam with a monochromatic one. This is an approximation that is commonly made in

CT image reconstruction. An accurate per-pixel energy calibration method will provide accurate values for the limits on the integral of 3.3 (for each pixel) in the polychromatic reconstruction problem. The image reconstruction has a fundamental impact on image quality. An accurate energy calibration reduces blurring in the energy domain and results in a better image reconstruction and an improved image.

3.5 Summary

- CT scanners reconstruct 3D volume images of an object from a series of 2D radiographic projections which are taken from various angles around the object. Conventional CT reconstructions represent the linear attenuation distribution of the respective object.
- The first commercial CT scanner, the EMI scanner, was produced in 1971. Dual-energy CT scanners typically use either dual-source or kVp-switching source methodologies. Multi-energy CT is capable of measuring 3+ energies, using photon counting detectors. The benefit of measuring energy information with multi-energy CT is that it enables information about the material composition of the object to be extracted from the data.
- Photon-counting energy-discriminating pixel detectors (PCXDs) are advantageous to charge-integrating devices in multi-energy CT. The energy discriminating features of PCXDs are based on the pulse heigh analysis of an incident x-ray and assigns it to several energy bins.
- Threshold dispersion in the Medipix3RX results in different effective threshold voltages of the analog discriminator which can be a limiting factor in global spectral resolution and the precision of energy calibration.
- The image reconstruction has a fundamental impact on image quality. The current image reconstruction in MARS CT approximates a polychromatic x-ray beam with a monochromatic one. This is an approximation that is commonly made in CT image reconstruction.
- An accurate energy calibration reduces blurring in the energy domain and results in a better image reconstruction and an improved image.

Chapter 4

X-ray fluorescence for energy calibration of the Medpix3RX

This chapter looks at initial modifications made to a per-pixel energy calibration method originally used by Panta *et. al.* [1]. The primary difference between the modified XRF method investigated here and the previous method is to measure the fluorescence photons that are found outside of the primary x-ray beam. This modification aims to increase the ratio of fluorescence photons to background photons remaining from the polychromatic x-ray beam.

Section 4.1 gives an overview of the XRF technique for the energy calibration of the detector and briefly discusses the motivation behind modifying the previous XRF method by Panta *et. al.*. The modified XRF is developed in section 4.2 and the results are discussed in section 4.3. Section 4.4 gives a summary of the main ideas in the chapter.

4.1 Overview and previous XRF calibration method

The potential of energy-discriminating photon-counting detectors (PCXDs) in medical x-ray imaging has been explored since the mid-nineties, the energy response of the energy-discriminating PCXDs are complex and need to be well calibrated in order to provide good image reconstructions (Equation 3.3). A per-pixel energy calibration technique for the Medipix photon-counting detector has been previously investigated by members of the MARS team [1]. The proposed technique will provide a powerful tool to determine the energy response of each of the pixels composing the detector, individually.

Calibrating the energy response of PCXDs (like the Medpix3RX) can be achieved using monochromatic photon sources, such as radio-isotopes or synchrotron sources [45–48].

Each of these methods have limitations that reduce their usefulness, such as availability, setup of equipment, long measurement time, and the large physical space needed to maintain the required geometrical set-up. X-ray fluorescence (XRF) is a good source of calibration spectra with well-defined photon energies (monochromatic source). The monochromatic x-ray spectra at various energies can be easily generated using various fluorescent materials [34, 49, 50].

The XRF is generated from the interaction between an x-ray beam and high atomic number targets. When the target is bombarded with x-rays of energies equal to or higher than the binding energies of the inner electrons of the target, the atoms in the target become ionised, creating electronic vacancies in the inner shells of the target atom. These electronic vacancies are filled by free electrons from the outer shells, resulting in the release of fluorescent photons with the same energy as the difference in energy between the respective inner and outer shells of the atom. The XRF is specific to an element as the energy levels of electrons in an atom have fixed orbital energy states.

Panta *et.al.* investigated a technique for the energy calibration of the Medipix3RX detector based on the monochromatic fluorescence photons emitted from different metal targets (XRF technique). The foil group modified Panta *et.al.*'s method slightly by measuring the fluorescence photons that are found outside of the primary x-ray beam to improve the fluorescence signal obtained from the metal foils. Satisfactory results were not obtained due to some of the metal foils being too thick.

The XRF energy calibration method used by Panta *et. al.* can be broken into two steps: (1) the fluorescence measurements and (2) using the fluorescence measurements to map the DAC steps to their energy response (keV).

Step 1: Fluorescence measurements

Different metallic foils of Mo, Pd, In, Ta, Pb with 100 - 300 μm thickness were used to generate the XRF signal. In separate measurements, each foil was placed on the front face of the MARS camera, as shown in Figure 4.1.

The x-ray tube was used to irradiate Mo, Pd, In, Ta and Pb at different kVp's of 30, 35, 40, 70 and 90, respectively. The reason for using different kVp's for each foil was to optimise the signal-to-noise ratio (SNR) in the main beam by maximising XRF and minimising Bremsstrahlung and scattering from direct exposure. The tube current and exposure time were adjusted to get between 1500 - 2000 photon counts per pixel in each measurement. Measurements were obtained by scanning across a broad range of DAC values for each counter (Figure 4.2).

Step 2: Mapping DAC to keV

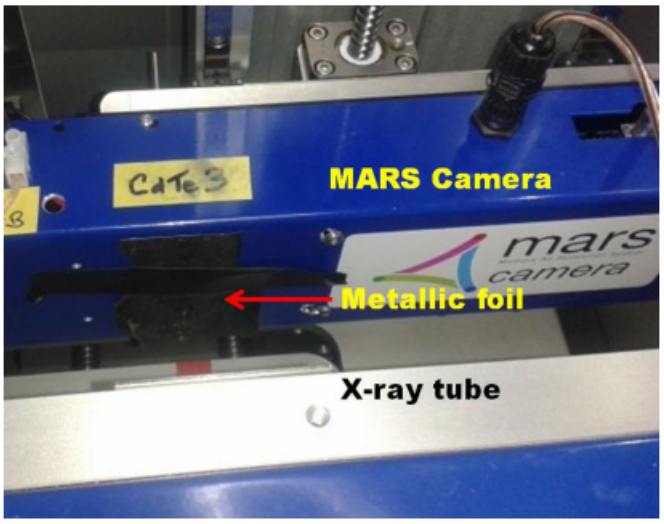

FIGURE 4.1: Experimental setup for measuring XRF from metallic targets by irradiating with polychromatic x-rays from x-ray tube. Image retrieved from Panta *et. al.* (2014) [1].

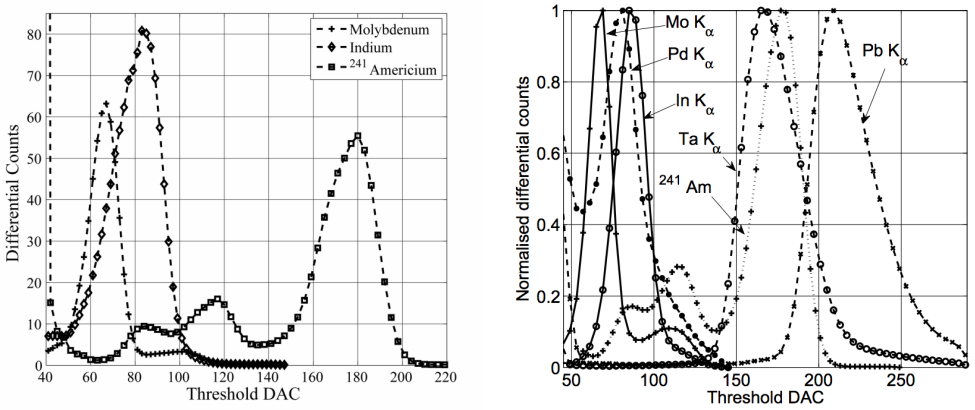

FIGURE 4.2: Energy calibration of the CdTe-Medipix3RX in CSM. (a) Energy response function of a pixel measured with XRF of Mo and In and (b) Energy response function of a pixel measured with XRF of Mo, Pd, In, Ta and Pb. Note that this is a normalised differential plot that has also been normalised. Image retrieved from Panta *et. al.* (2014) [1].

The threshold DAC corresponding to the K_α peaks for a particular pixel are the points that are used in the energy calibration of that pixel. Each foil is used to produce an energy calibration point by assigning the energy of the XRF peak to the respective threshold DAC. The threshold DAC and photon energy of the XRF peak should ideally show a positive linear relationship (Figure 4.3). The linear relationship between DAC and photon energy is calculated using a linear least squares regression, which is then used as the energy calibration of the respective pixel. For the calculated energy calibration to be accurate, foils of different elements are needed to provide reference energies across

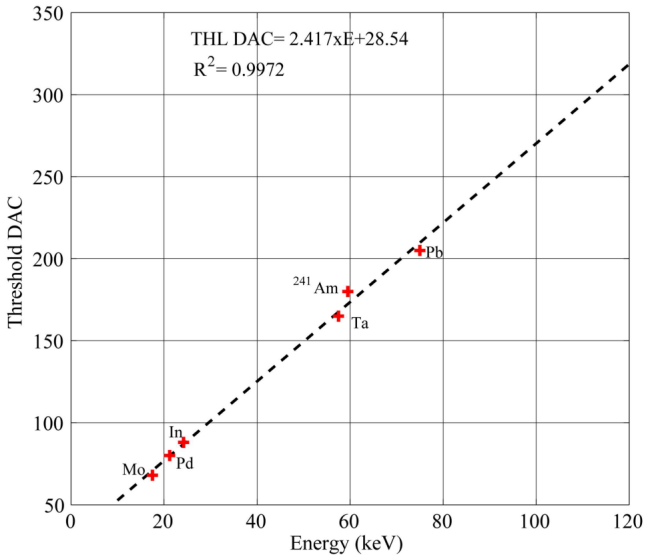

FIGURE 4.3: Establishing the relationship of threshold DAC at XRF peaks with corresponding energy for a pixel. A linear least squares regression was used. Image retrieved from Panta *et. al.* (2014) [1].

the wide energy range of interest.

The key features of the XRF calibration technique in Panta's work are listed below. Some of these features are changed in the modified XRF calibration method.

- Thick foils (100-300 μm) were used.
- The foils were manually mounted on the front face of the camera which means the technique, as it stands, is not automtable.
- Fluorescence is measured with the detector in the main beam path.

4.2 Modified XRF calibration technique

The modified XRF calibration technique is a continuation of the work done by Panta *et. al.* on the fluorescence measurements (Step 1) with some modification of the key features which include: (1) mounting the foils on the scanner filter bar which is mounted between the x-ray source and the collimators; and (2) measuring the XRF of molybdenum (Mo), Tantalum (Ta) and lead (Pb) foils with the detector out of the main beam path. The location of the foils will enable future automisation of the modified XRF calibration technique, which was the initial motivation behind this work. The XRF energies for relevant target foils are presented in Table 4.1.

Atomic number (Z)	Metallic targets	XRF ($K\alpha_1$) energy (keV)
42	Molybdenum (Mo)	17.48
73	Tantalum (Ta)	57.53
82	Lead (Pb)	74.97
49	Indium (In)	24.21
60	Neodymium (Nd)	37.36
66	Dysprosium (Dy)	46.00

TABLE 4.1: XRF $K_{\alpha 1}$ energies from various metallic targets (foils)

The MARS version 5 scanner (MARS-CT11) was used for the modified XRF calibration technique. The software is able to move each filter on the filter bar in and out of the main beam. The filter bar can contain many filters (such as air, 1mm Al, 2mm Cu) and two examples are shown in Figure 4.4. The filter bar is positioned between the x-ray source and detector, approximately 5 cm from the x-ray source and 90 cm away from the detector. The filter bar used by the foil group has three pieces of metal foils glued to it, as shown in Figure 4.4a. In future experiments the filter bar will have the ability to select one out of six foil materials, as shown in Figure 4.4b. The collimators are located after the filter bar and select the correct foil on the filter bar so that the appropriate XRF of each foil travels to the detector.

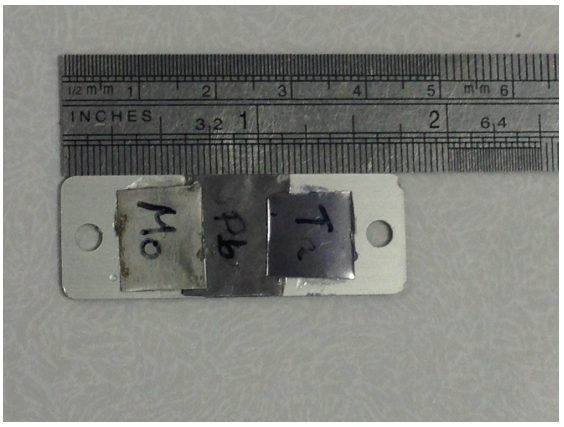

(A) Filter element with Mo, Pb and Ta foils attached.

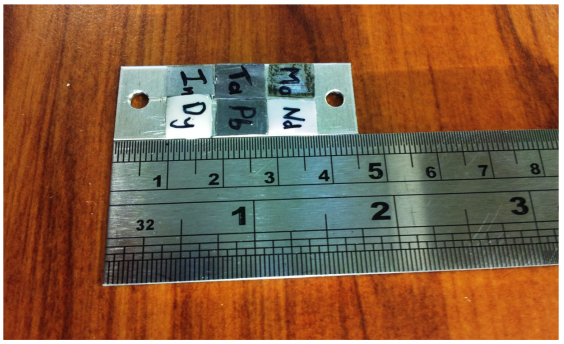

(B) Filter element with Mo, Pb, Ta, Nd, In and Dy foils attached.

FIGURE 4.4: Filter elements for current (A) and future (B) experiments.

The monochromatic fluorescence photons from the different targets are emitted isotropically for each atom but mostly escape from the foil in the forward and backward direction. In order to avoid the primary beam, the detector is moved out of the main beam by changing the camera translation using the MARS Graphical User Interface (GUI). Each different foil requires a different camera translation. Figure 4.5 provides a geometric representation of the collimator and camera translation for the molybdenum foil.

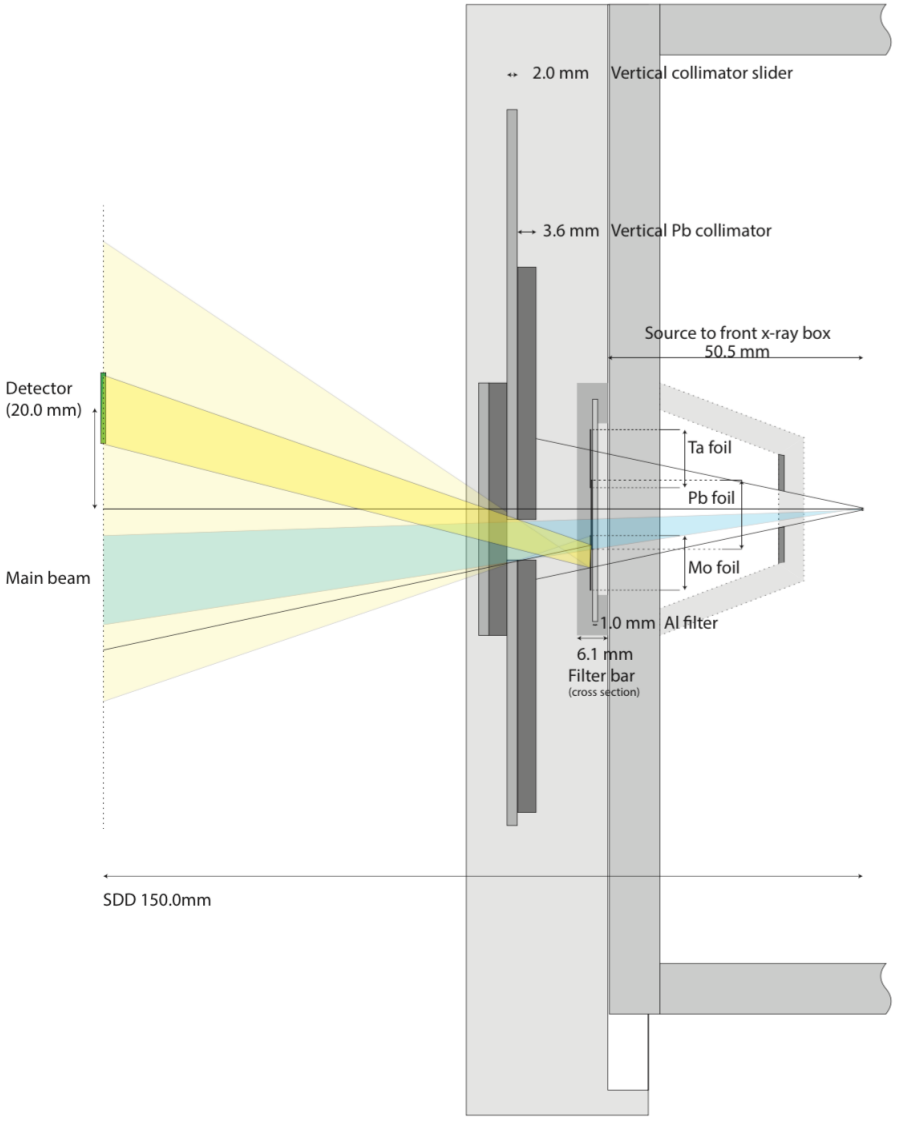

FIGURE 4.5: Experimental set-up for the molybdenum foil. The blue beam represents the main beam coming from the x-ray source. The fluorescence is spread out both in, and away from, the main beam. The collimators are chosen so that the yellow region will only contain fluorescence from one foil (Mo, Ta or Pb) and the detector is moved up to the yellow region to detect the fluorescence. Similar geometric diagrams were constructed for tantalum and lead [9].

In summary, the following steps were taken for measuring the XRF from each foil:

1. The collimators are positioned so that the correct foil on the filter bar is selected but they do not show up in an image of the main beam. The current and exposure time are kept low during this step.
2. The camera translation is adjusted so that the detector is capturing images that are just out of the main beam.
3. Since the detector is out of the main beam the current and exposure time can be increased. Correct beam parameters are established and the fluorescence spectra is obtained.

A threshold scan was used to acquire the distribution of photons over a range of energy thresholds. The threshold scan was performed by gradually increasing the threshold DAC to acquire the number of photon events as a function of the applied threshold DAC over the range of interest. The threshold DAC step was 3, which corresponds to an average step of 0.75 keV. The tube current was 350 μA, 350 μA and 300 μA with tube voltages of 40V, 40V and 95V for Mo, Ta and Pb, respectively. The detector was moved up 20 mm for Mo, down 10 mm for Ta, and up 20 mm for Pb. The horizontal and vertical collimator were also adjusted accordingly for each foil. A summary of the experimental parameters is shows in Table 4.2.

	Mo	Ta	Pb
Tube voltage (kVp)	40	40	95
Tube current (μm)	350	350	300
Camera translation (mm)	20	-10	20
Left (horizontal) collimators	2.7	2.7	2.7.
Right (horizontal) collimators	3	3	3
Top (vertical) collimators	-2	5	1.9
Bottom (vertical) collimators	10	-1	2.3

TABLE 4.2: X-ray beam parameters used by the foil group in the modified XRF technique.

4.3 Results

The differential photon counts versus DAC value shows the XRF spectra of random pixels in Figures 4.6, 4.7 and 4.8 for molybdenum, tantalum and lead, respectively. The Mo peak is not consistent across all pixels. The XRF peak for pixel (22, 73) and pixel (31, 16) are well defined and look useful. However, in pixel (96, 29) two different XRF peaks are observed and a single calibration point cannot be clearly defined. The spread

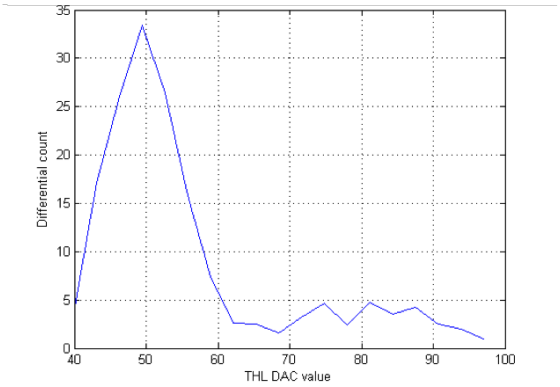

(A) Mo fluorescence scan for pixel (22,73)

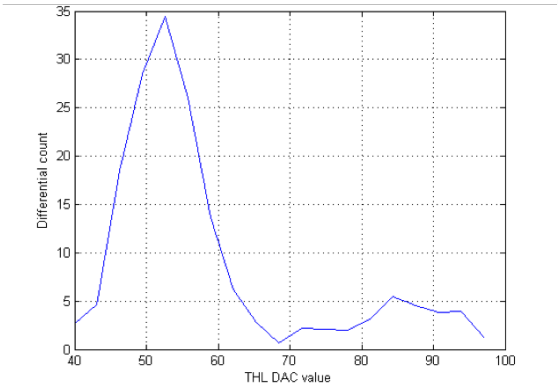

(B) Mo fluorescence scan for pixel (31,16)

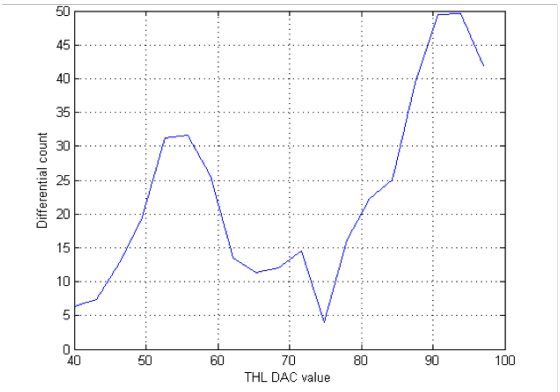

(C) Mo fluorescence scan for pixel (96,29)

FIGURE 4.6: Molybdenum fluorescence scan for specified pixels

of the Ta peak is large. The x-ray spectrum also shows a lot of inconsistent spikes and there is a lot of variation between the pixels. The Pb spectra shows a clear and well defined XRF peak for each pixel.

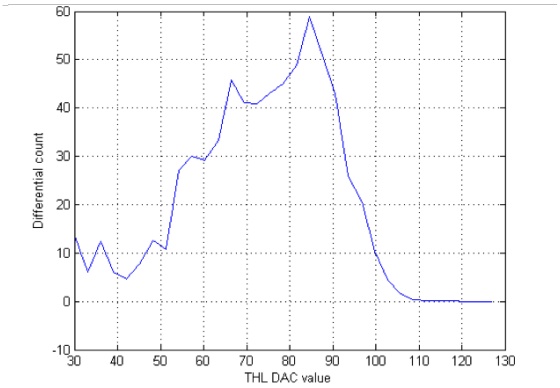

(A) Ta fluorescence scan for pixel (22,73)

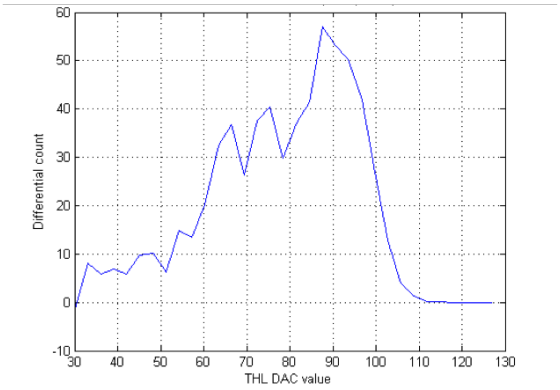

(B) Ta fluorescence scan for pixel (31,16)

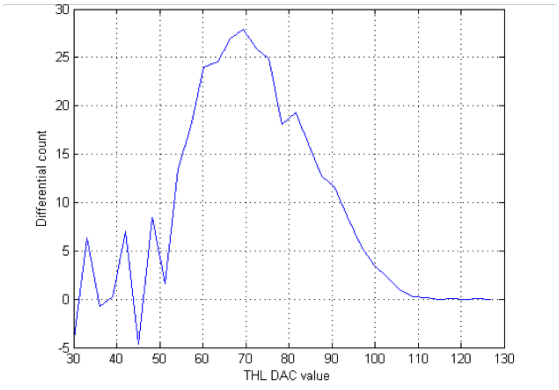

(C) Ta fluorescence scan for pixel (96,29)

FIGURE 4.7: Tantalum fluorescence scan for specified pixels

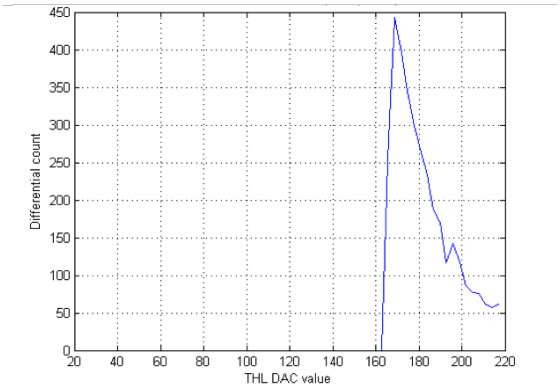

(A) Pb fluorescence scan for pixel (22,73)

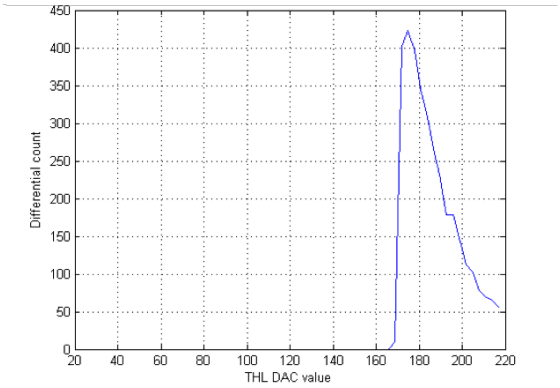

(B) Pb fluorescence scan for pixel (31,16)

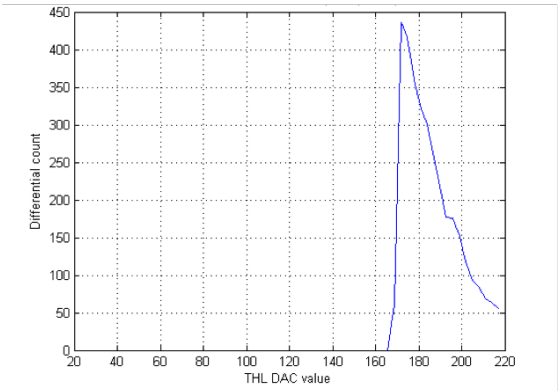

(C) Pb fluorescence scan for pixel (96,29)

FIGURE 4.8: Lead fluorescence scan for specified pixels

4.4 Discussion

The modified XRF technique mounted the foils on a filter bar between the x-ray source and the detector, but out of the direct x-ray beam. Collimators were used to select the characteristic x-rays from one foil at a time. In this set-up some fluorescence was observed. However, the XRF peaks were not as well-defined as was expected and a clear energy calibration point could not be established for the Mo (Figure 4.6) and Ta (Figure 4.7) foils. The XRF peaks in the work done by Panta *et. al.* (Figure 4.2) are better defined than for the modified XRF technique.

The Mo peak in Figure 4.6 is not consistent across all pixels. The XRF peak for pixel (22, 73) and pixel (31, 16) are well defined and look useful. However, in pixel (96, 29) two different XRF peaks are observed. It is unlikely that the reason for this is due to the Cd or Te fluorescence from the detector. Pixel (96, 29) could be a malfunctioning pixel, however, further experimentation is required to verify this. The spread of the Ta peak in Figure 4.7 is large, not well defined, and is jagged. The XRF peak for pixel (96, 29) is a little more well-defined, however, that is the pixel that shows inconsistent results for Mo. The Pb spectra shows clear and well-defined XRF peaks for each pixel.

The thickness of the foils that were used in the previous XRF calibration method by Panta *et. al.* and in the modified XRF calibration method were 300 μm. Each foil has a different atomic number, Z and the likelihood of a photoelectric event occurring, and thus the likelihood of a fluorescent photon being emitted, depends on the fourth or fifth power of Z (depending on the beam energy). A photoelectric absorption is most likely to occur just above the K-edge of a material (K_α). Mo and Ta have relatively low atomic numbers and K_α values which means that they have low penetrability. In order for a maximum fluorescence signal to escape, the Mo and Ta foils must be thin. The Pb foil, on the other hand, has a much higher atomic number and K_α value and so a thicker foil is needed to absorb the higher energy x-rays. However, all of the foils in previous and modified XRF methods have foil thicknesses of 300 μm, regardless of their atomic number and K_α energies. Chapter 5 investigates what the optimal thickness for each of these foil materials is to both assist with the interpretation of the initial foil group experiments using the modified technique, and to improve the experimental design for future testing.

Another consideration for the design of future experiments is that the sensor layer of the detector also contains K_α fluorescence peaks which can be used in the energy calibration. For example, the Medipix3RX used in these experiments has a CdTe sensor layer, and we see Cd (23.17 keV) and Te (27.47 keV) fluorescence peaks in every measurement [Personal communication from P. Butler in June 2014]. These sensor layer fluorescence

peaks occur from the fluorescence photons created by a higher energy photon interacting with the sensor layer, travelling far enough away from the primary interaction of the incoming photon to be measured in a separate pixel. These peaks are therefore generally observed to be smaller than the peaks obtained for foil fluorescence, as can be seen in the work by Panta *et. al* (Figure 4.2). The presence of sensor layer fluorescence peaks in the results of a foil fluorescent measurement also means that some of the K_α photons have been measured by the detector as having a lower energy (i.e some K_α photons escape into other, usually neighbouring, pixels taking their energy with them). This means that for the CdTe detector there are potentially up to five calibration points that can be obtained from a single foil. This is a useful property to consider for future implementation.

4.5 Summary

- Calibrating the energy response of PCXDs (like the Medpix3RX) can be achieved using monochromatic photon sources, such as radio-isotopes or synchrotron sources, however, these have limitations. X-ray fluorescence (XRF) is a good source of calibration spectra with well-defined photon energies.
- The monochromatic x-ray spectra at various energies can be easily generated from interaction between an x-ray beam and a high atomic number target.
- A per-pixel energy calibration technique for the MARS scanner using XRF was previously discussed by Panta *et. al.*. The XRF energy calibration method can be broken into two steps: (1) the fluorescence measurements and (2) using the fluorescence measurements to map the DAC steps to their energy response (keV).
- The modified XRF calibration technique was based off the technique used by Panta *et. al.* with some modification of the key features which include mounting the foils on the scanner filter bar and measuring the XRF with the detector out of the main beam path. These features were intended to improve the fluorescence signal obtained from the metal foils, however, the results were not as expected.
- One of the potential causes of this (foil thickness) is investigated in the following chapter.

Chapter 5

Determination of optimal foil thickness

The primary concern of this chapter is to develop a model that determines the optimum foil thickness at which the fluorescence signal, in the modified XRF method, is maximised.

An overview to the chapter in terms of photoelectric interactions in the foil is given in section 5.1. Photon absorption and the fluorescent yield is discussed in section 5.2. The probability of a K_α fluorescent photon being emitted is outlined in section 5.3. Section 5.4 defines some of the parameters used in the simple model for determining optimum foil thickness, which is developed in section 5.5. Section 5.6 develops a model optimising the foil thickness for the average energy of a photon beam, and section 5.7 introduces the energy integrating model. Section 5.8 discusses the results of both models and section 5.9 gives a summary to the chapter.

5.1 Overview

X-ray interactions form the basis for image reconstruction in a CT scanner. Recall that in a photoelectric interaction a photon transfers all its energy to an electron located in one of the atomic shells. The orbital electron is consequently ejected (as long as the incident energy is greater than its binding energy) and very soon after an electron from a higher shell drops to fill this vacancy. This results in the release of a photon, which represents the characteristic or fluorescence radiation of the target material. Chapter 4 describes an experiment, which I participated in, where foils of three pure metals were

irradiated with a polychromatic x-ray beam, creating fluorescence photons which were used to calibrate the detector.

5.2 Photon absorption in the foil

A material with a high atomic number Z has a higher electron density, and thus a photon passing through it is likely to undergo more interactions. The energy of the incident photon beam and the atomic number determine which type of photon interaction is most likely to happen. In particular above about 30 keV where the predominant interaction is the photoelectric interaction between the photon and those orbital electrons whose binding energy is closest to the photon energy. To increase the number of fluorescence photons being created a higher number of photoelectric interactions are required. Two models optimising the fluorescence signal are developed in this chapter. One is a simple model that makes approximations of a monochromatic beam and the other is an energy integrated model.

The photoelectric absorption contribution to the linear attenuation coefficient is given by τ (Equation 2.4), where the intensity of the photon beam decreases with increasing distance through a material, d, as $e^{-\tau d}$ and is a function of the atomic number of the target atom and photon energy. The tables of the photoelectric absorption probability were originally based on experiment. Nowadays they are based on the solution of the Schrödinger equation in the dipole approximations using self-consistent field wave functions.

The probability of the photoelectric effect decreases with increasing photon energy, however, for every element the probability of the photoelectric effect as a function of photon energy exhibits sharp discontinuities called absorption edges, as shown in Figure 5.1. This sharp jump in attenuation occurs at the electron shell binding energies as there are more electrons available to undergo photoelectric interactions and a closer match of the photon energy to the binding energy. The probability of interaction for photons of energy just above an absorption edge is much greater than that of photons of energy slightly below the edge.

5.2.1 Fluorescence yield

In photoelectric absorption, an electron transition does not always result in the production of a characteristic x-ray (fluorescence). There is also a competing process known as Auger electron emission. The probability that the electron transition will result in

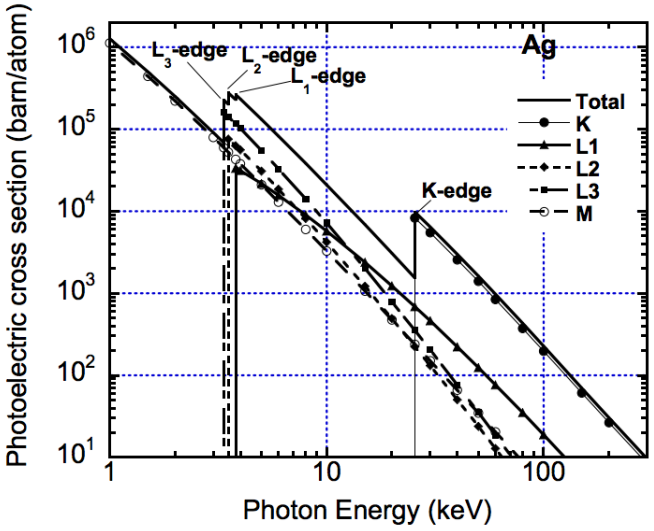

FIGURE 5.1: A plot of the photoelectric cross-section versus photon energy exhibits characteristic absorption edges for Ag. Figure retrieved from Cullen *et. al.* (1989) [51].

the emission of a characteristic x-ray is called the fluorescent yield ω_f. The precise definition of ω_f has changed over time [52–54]. The 1918 paper by Barkla [55] introduced the concept of fluorescence yield, defining it as the ratio of the energy carried by the fluorescence radiation to the energy carried by the radiation absorbed in a sample. The present day definition of fluorescent yield is defined as the probability that a vacancy of an atomic shell or sub-shell is filled through a radiative transition.

A fluorescence photon emitted from the K-shell as a result of a photoelectric interaction in an adjacent shell is called a K_α fluorescence photon. The probability of a K_α fluorescence photon being emitted is given by:

$$\omega_{K_\alpha} = \frac{\text{Number of K}_\alpha \text{ fluorescent photons}}{\text{Number of K-shell interactions}} \tag{5.1}$$

The K-shell fluorescent yield is essentially zero for elements $Z < 10$ (i.e., the elements comprising the majority of soft tissue), about 15% when $Z = 20$ (calcium), about 65% for $Z = 53$ (iodine) and approaches 80% for $Z > 60$.

5.3 Probability of K_α fluorescence

The probability that an x-ray photon interacts in the foil and is attenuated through a photoelectric interaction with the K-shell is

$$P_K = \frac{\tau_K(E)}{\mu(E)} \tag{5.2}$$

where τ_K is the K-shell photoelectric interaction component of the foil's linear attenuation coefficient (note that $\tau_K \neq \tau$) and μ is the full attenuation coefficient of the x-ray beam (Equation 2.4). We can obtain the probability of a photon interaction causing a K_α fluorescence event, P_{K_α}, by multiplying the probability of a K-shell interaction by the fluorescence yield.

$$P_{K_\alpha} = \omega_{K_\alpha} \times \frac{\tau_K}{\mu(E)} \tag{5.3}$$

5.4 K-shell photoelectric attenuation coefficient

To calculate P_{K_α} the K-shell photoelectric component of the linear attenuation coefficient, τ_K is needed. The τ_K values for the three foils used in the experiment was obtained from Scofield (1973) [56].

Only a small number of coefficients were available for each material, in the diagnostic imaging range. To approximate the τ_K for photon energies between the available coefficients a linear interpolation was done on the log of the coefficients, using MATLAB (as shown in Figures 5.2 5.3 and 5.4). These τ_K are compared to the full linear attenuation values which were obtained from the NIST XCOM database [57]. The reason the linear interpolation was done on $\log\tau_K$ instead of τ_K was to obtain a better approximation to the curvature of $\tau_K(E)$. The associated plots are shown below.

5.5 Simple model for determining optimal foil thickness

We first develop a simple model that looks at the number of fluorescence photons escaping a foil using a monochromatic input x-ray beam. It considers how many K_α fluorescence photons are created by the input photons in every depth into the foil, and the probability that those fluorescence photons can travel the remaining thickness of the foil, and the probability that those fluorescence photons can travel the remaining thickness of the foil without being attenuated.

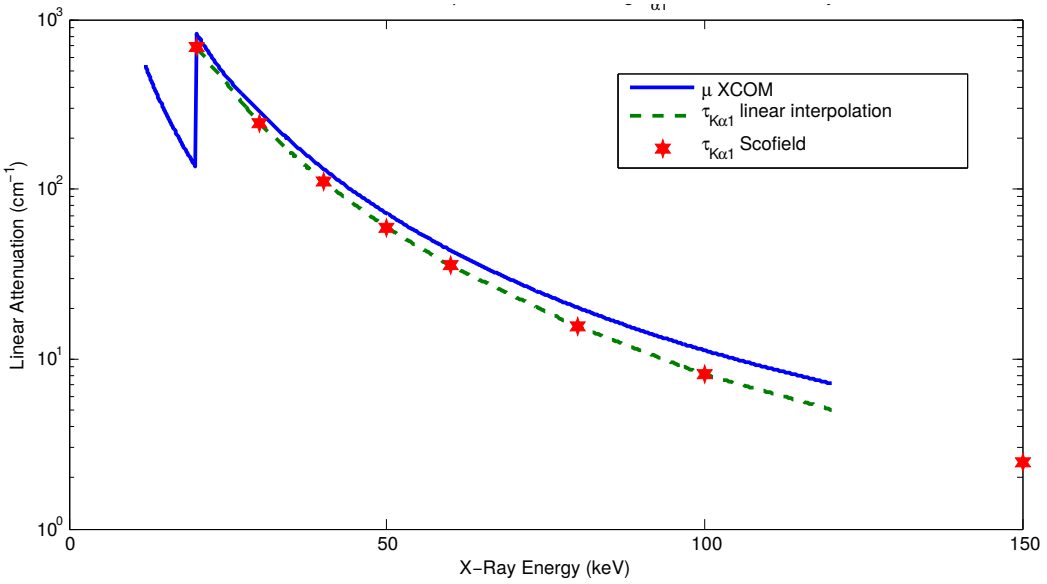

FIGURE 5.2: Linear attenuation component for generating $K_{\alpha 1}$ fluorescence for molybdenum.

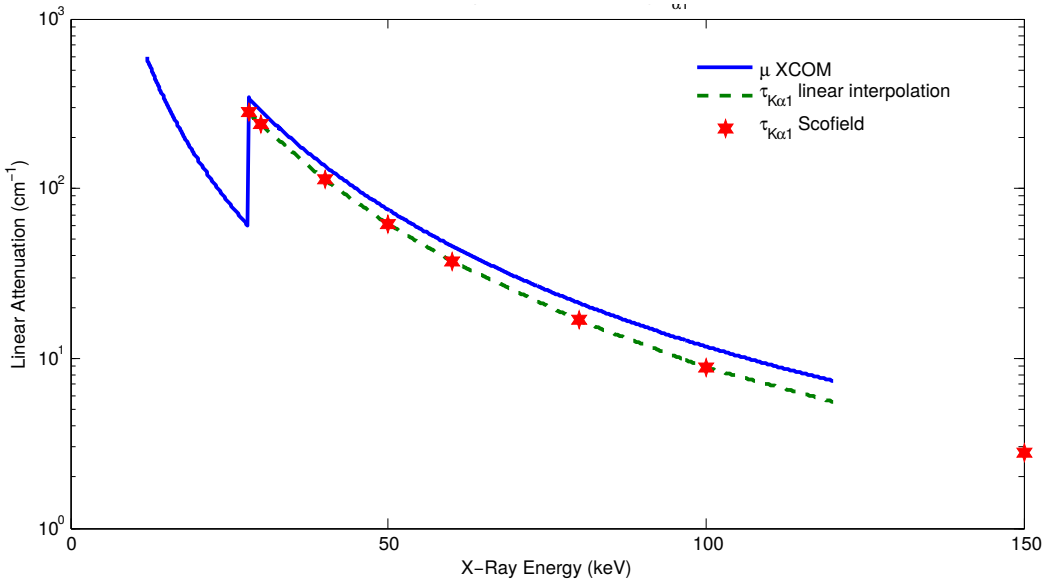

FIGURE 5.3: Linear attenuation component for generating $K_{\alpha 1}$ fluorescence for indium.

5.5.1 Number of K_α photons escaping a foil of thickness L

The number of fluorescent photons escaping a foil $N_{K_\alpha}(L, E)$ of thickness L when using a monochromatic input x-ray beam of energy E is given by:

$$N_{K_\alpha}(L, E) = \int_0^L P_{K_\alpha} N(x) e^{-\mu_{K_\alpha}(L-x)} dx \tag{5.4}$$

$$= \int_0^L \omega_{K_\alpha} \tau_{K_\alpha}(E) I_0(E) \mu(E) e^{-\mu(E)x} e^{-\mu_{K_\alpha}(L-x)} dx \tag{5.5}$$

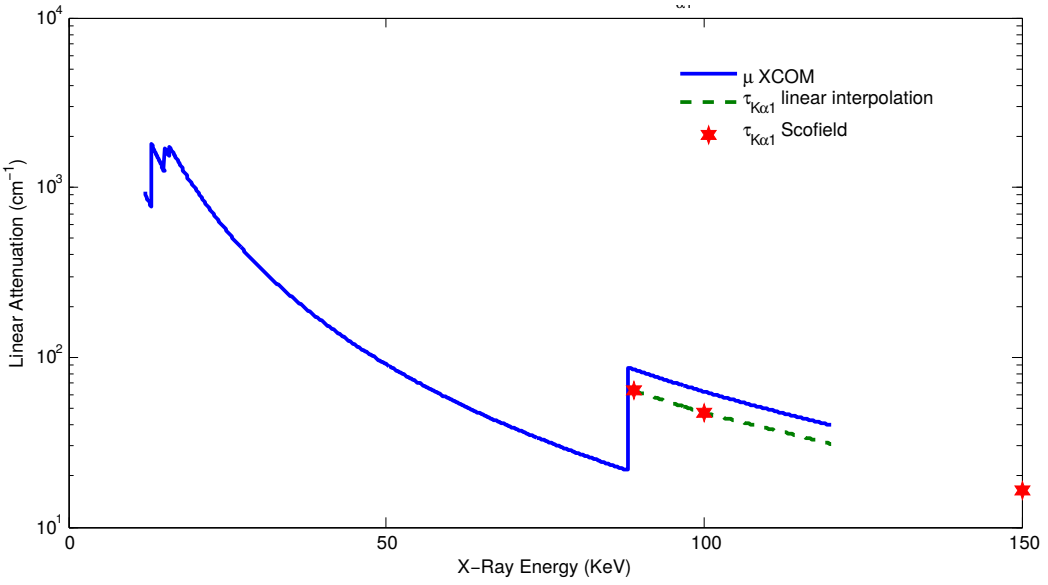

FIGURE 5.4: Linear attenuation component for generating $K_{\alpha 1}$ fluorescence for lead.

where

- $P_{K_\alpha} = \omega_{K_\alpha} \times \tau_{K_\alpha}(E)/\mu(E)$ gives the fraction of those attenuated photons which generate K_α photons events.
- $N(x) = I_0(E)\mu(E)e^{-\mu(E)x}$ is the number of x-rays that are attenuated from the main beam in some infinitesimal thickness dx at some position $\in [0, L]$ in the foil. This result is given by differentiating the negative of the Beer-Lamber law with respect to distance.
- $e^{-\mu_{K_\alpha}(L-x)}$ gives the fraction of those fluorescent photons which escape the foil. Hence μ_{K_α} is the attenuation coefficient of the foil for the fluorescent photons.
- This is integrated over all distances $x \in [0, L]$ in the foil where fluorescent photons can be created.

Calculating the integral then gives:

$$N_{K_\alpha}(L, E) = \omega_{K_\alpha} I_0(E) \frac{\tau_{K_\alpha}(E)}{\mu_{K_\alpha} - \mu(E)} \left[e^{-\mu(E)L} - e^{-\mu_{K_\alpha} L} \right] \tag{5.6}$$

This can be simplified further by grouping the $\omega_{K_\alpha} I_0(E)$ terms into a single constant A (remembering that we are dealing with the monochromatic input beam).

$$N_{K_\alpha}(L, E) = A \times \frac{\tau_{K_\alpha}(E)}{\mu_{K_\alpha} - \mu(E)} \left[e^{-\mu(E)L} - e^{-\mu_{K_\alpha} L} \right] \tag{5.7}$$

The $\tau_{K_\alpha}(E)/(\mu_{K_\alpha} - \mu(E))$ was not absorbed into the constant as the sign of this term, and the exponential term, changes depending on whether or not $\mu(E) > \mu_{K_\alpha}$ in calculating $N_{K_\alpha}(L, E)$.

5.5.2 Analysis step: How does the number of fluorescence photons change with foil thickness?

After each photoelectric interaction, the number of fluorescence photons will decrease as they travel through the thickness of the foil. A plot of the number of fluorescent photons (K_α) at varying foil thicknesses was plotted for Mo, In and Pb foils. Values were entered into Equation 5.7 to obtain these plots. The NIST XCOM database gives values for the mass attenuation coefficients, the K_α values and the densities, ρ, of each foil material (at room temperature) [57], as shown in Table 5.1.

The monochromatic energies are selected based on the K-edge of the material. The fluorescence signal is seen to be at a maximum just above the K-edge of a material, therefore the first energy selected lies just above the K-edge of the material. The final energy is about four times the first energy, with the remaining middle two energies being approximately evenly spaced between the two extremes. (Note that because the K-edge for lead is 75 keV and the maximum energy of the tube is 120 keV the energies that were chosen for lead are just a range of energies spread between the K-edge and 120 keV.)

Foil	K-edge (keV)	K_α (keV)	$(\mu/\rho)_{K_\alpha}$ cm^2g^{-1}	ρ_{foil} room temp.	μ_{K_α} cm^{-1}
Mo	20.00	17.48	18.85	10.28	193.78
In	27.94	24.21	12.23	7.31	89.40
Pb	88.00	74.97	2.85	11.34	32.32

TABLE 5.1: The K-edge, K_α and attenuation parameters for the molybdenum, indium and lead.

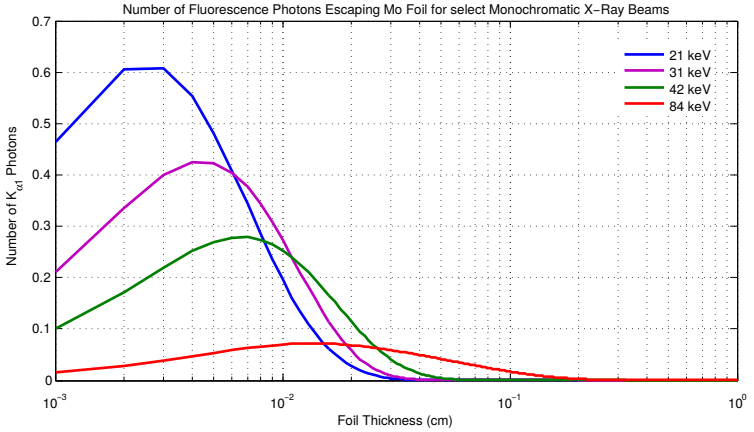

FIGURE 5.5: Number of fluorescent photons escaping Mo foil for selected monochromatic x-ray beams.

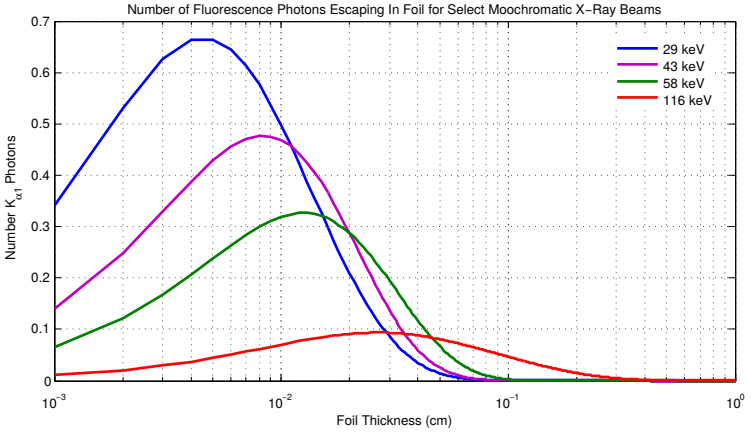

FIGURE 5.6: Number of fluorescent photons escaping In foil for selected monochromatic x-ray beams.

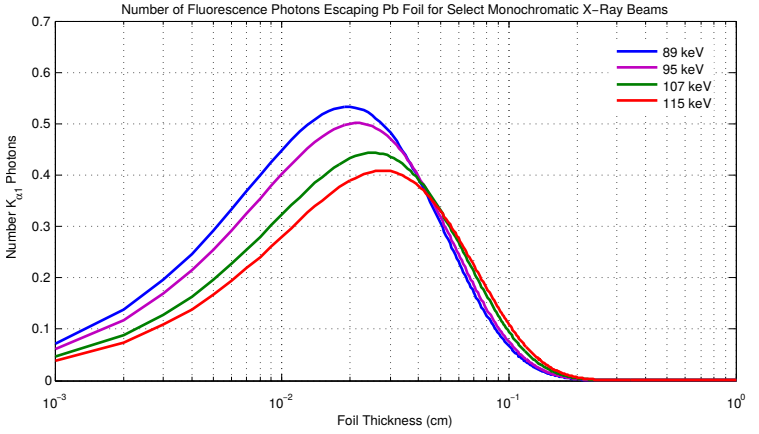

FIGURE 5.7: Number of fluorescent photons escaping Pb foil for selected monochromatic x-ray beams.

The general trend that we see from these figures is that higher energy photons require thicker foils. This is because higher energy incident photons on average travel further before they interact. There are fewer high energy photons than low energy photons in the source spectrum, so in terms of absolute number of fluorescence photons we expect to need thicker foils. Thick foils are optimal for high energy photons as they absorb most of the fluorescence produced by low energy photons. The energy integrating model will take this fact into account (see the next section).

Other important features to note on these plots include:

- The maximum, for each energy, is at the thickness where the most fluorescence photons will escape the foil
- Left of the maximum is where the input photons are most likely escaping before they can generate fluorescence.
- Right of the maximum is where input photons are mostly generating fluorescence, but the fluorescence is being mostly absorbed within the foil before it escapes.

5.5.3 The optimal foil thickness $L^*(E)$ for monochromatic input

The optimum foil thickness is obtained at the maximum number of K_α photons, shown as the peak in Figures 5.5, 5.6 and 5.7. This can be obtained by differentiating Equation 5.7 with respect to foil thickness L and setting the result equal to zero. Thereby we obtain an analytic formula for the optimal foil thickness $L^*(E)$ which will allow maximum fluorescence to escape.

$$L^*(E) = \frac{1}{\mu(E) - \mu_{K\alpha}} \times \ln\left(\frac{\mu(E)}{\mu_{K_\alpha}}\right) \tag{5.8}$$

The optimum foil thickness for the monochromatic input beam is shown in Figure 5.8.

5.6 Optimising foil thickness for the average beam energy

In this step the optimum foil thickness, using the effective energy of the component of the beam that is above the K-edge, is calculated. The effective energy is the average energy per photon of a polychromatic x-ray beam calculated as if it were monochromatic [58]. The effective energy is just an average of all energies in the x-ray beam which are weighted by the normalised input x-ray spectrum. However, we are only interested in

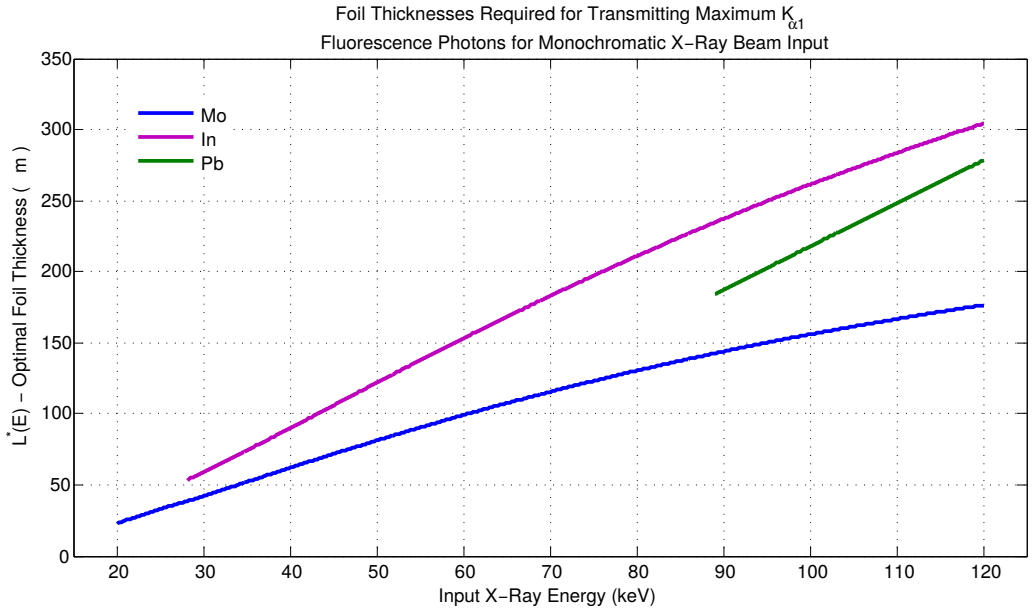

FIGURE 5.8: Optimum foil thickness for monochromatic input beam. Note that each curve starts at the K-edge energy for the respective material

the x-rays that have energies high enough to generate fluorescence and so the effective energy will be:

$$E_{eff} = \int_{K-edge}^{E_{max}} \left[\frac{I_0(E)}{\int_{K-edge}^{E_{max}} I_0(E)dE} \times E \right] dE \tag{5.9}$$

The results of this calculation for Mo, In and Pb are shown in the table below.

Foil	Mo	In	Pb
E_{eff} (keV)	54.14	56.58	99.19
$L^*(E_{eff})$ (μm)	89	142	215

TABLE 5.2: Optimal foil thickness at the effective energy of the beam for the simple monochromatic model

5.7 Energy integrating model

When we use a polychromatic x-ray beam (such as in the foils experiment) we need to consider that there are varying amounts of photons of different energies which, on average, interact at different depths in the foil. To improve on the above approximation that uses the effective energy of the beam, the total escaping fluorescence is calculated

by integrating Equation 5.6 over all x-ray energies present in the x-ray beam.

$$N_{K_\alpha}(L) = \int_0^{E_{max}} \omega_{K_\alpha} I_0(E) \frac{\tau_{K_\alpha}(E)}{\mu_{K_\alpha} - \mu(E)} \left[e^{-\mu(E)L} - e^{\mu_{K_\alpha} L} \right] dE \tag{5.10}$$

The attenuation and x-ray spectrum terms are sufficiently complicated to be problematic so the integral is solved numerically by approximating as a sum with ΔE=0.1 keV. Equation 5.10 is modified to:

$$N_{K_\alpha}(L) = B \times \int_0^{E_{max}} I_0(E) \frac{\tau_{K_\alpha}(E)}{\mu_{K_\alpha} - \mu(E)} \left[e^{-\mu(E)L} - e^{\mu_{K_\alpha} L} \right] dE \tag{5.11}$$

where B is a constant containing ω_{K_α} and the inverse of some normalisation factor used on I_0 (the maximum value of I_0 is used for the normalisation). We will ignore B in our calculation because we do not need to know the absolute photon counts at this stage. However, it could be useful to implement this factor in future work.

For this numerical integration the same x-ray spectrum from the foil group experiments is used, and again the other tube and set-up parameters are absorbed into the constant B (which is ignored). Then the transmitted fluorescence for each foil, at thicknesses ranging from 0 cm to 1 cm, are calculated. This is the same type of plot that was produced previously for the monochromatic case (Figures 5.5, 5.6 and 5.7).

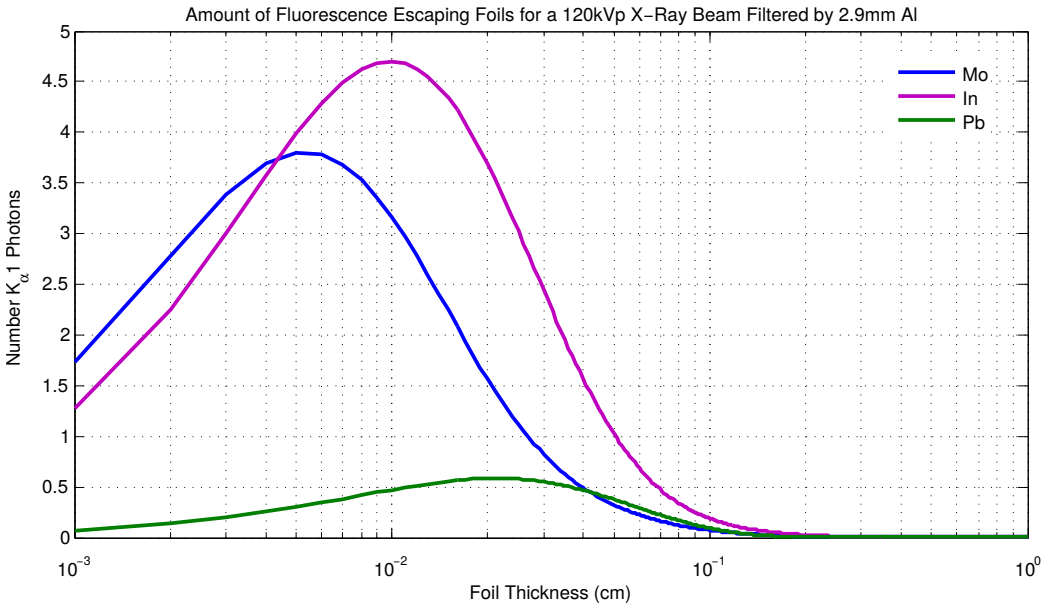

FIGURE 5.9: Optimum foil thickness for polychromatic input beam. Note that this is not the true counts from the parameters used in the foils experiment, certain parameters have had a multiplicative constant pulled out and ignored to make the calculation simple. The x-ray spectrum has been normalised.

From these values the optimum thickness for Mo, In and Pb foils can be seen to be

Foil	Mo	In	Pb
L^* (μm)	50	100	210

TABLE 5.3: Optimal foil thickness for the different foils using the polychromatic energy integrating model

5.8 Discussion

Two mathematical models optimising the fluorescence signal coming from the foils were developed: (1) the simple model for determining optimal foil thickness assumes a monochromatic beam and calculates the optimum foil thickness at specific energies; and (2) the energy integrating model is a polychromatic model that uses numerical integration across all energies to give the foil thickness at which a maximum fluorescence signal is detected.

Recall that the initial foil group experiments used foil thicknesses L of 300 μm for each foil (Mo, Ta and Pb). A well defined peak was obtained for lead in the modified XRF experiment because its thickness, L, was not too far off the L^* estimated by the polychromatic model. The Mo foil did not show well defined peaks in the initial experiments and it can be concluded from the results of the optimal foil thickness calculations that the foils used were much too thick. The next step for the foil group is to repeat the previous experiments using foils made to the optimum thicknesses predicted in this work.

Another important point to note is that the steepness of the peaks in Figure 5.9 give a measure of how much tolerance there is on the foil thickness, i.e. if the maximum is a sharp narrow peak then a small change in thickness will cause a large change in fluorescence output, and on the other hand if the peak is broad then a difference in foil thickness may have little effect on the transmitted fluorescence. The lead foil has more tolerance than the molybdenum and tantalum foils. This is related to the energy of the fluorescence photon, lower energies get absorbed across shorter distances.

A comparison of the optimum foil thickness for both the simple and the energy integrating model is shown in Table 5.4. There is quite a difference between the results of the two models, particularly for the foils with low effective energies (such as Mo). This demonstrates why using E_{Eff} in approximating a polychromatic beam in the monochromatic model will obtain a thicker foil than the optimum for foils with lower energy. The Pb K-edge to E_{max} spans a smaller energy range (Figure 5.8).

Foil	Mo	In	Pb	Ta	Nd	Dy
K_α (keV)	17.48	24.21	74.97	57.53	37.36	46.00
$L^*(E_{eff})$ (μm)	89	142	215			
L^* (μm)	50	100	210			
Experimental thickness (μm)	300		300	300		

TABLE 5.4: Comparison of optimal foil thickness parameters and results for Mo, In, Pb, Ta, Nd and Dy.

5.9 Summary

- An incident x-ray photon will have a certain probability that it will interact with the atoms of the foil via a photoelectric interaction. The photoelectric absorption contribution to the linear attenuation coefficient is given by τ which decreases with increasing distance through a material d as $e^{-\tau d}$ and is a function of atomic number of the target atom and photon energy.

- A fluorescence photon emitted from the K-shell as a result of a photoelectric interaction in an adjacent shell is called a K_α fluorescence photon.

- The fluorescent yield, ω_f, is defined as the probability that a vacancy of an atomic shell or sub-shell is filled through a radiative transition.

- The probability of a photon interaction causing a K_α fluorescence event, P_{K_α}, is the product of the probability of a K-shell interaction by the fluorescent yield.

- The simple model for determining optimal foil thickness is a monochromatic model that approximates the number of K_α photons escaping a foil of thickness L.

- The effective energy, E_{Eff}, of the x-ray beam is used to determine how the number of fluorescence photons change with foil thickness.

- When we use a polychromatic x-ray beam (such as in the foils experiment), there are varying amounts of photons of different energies which, on average, interact at different depths in the foil. To calculate the total escaping fluorescence the energy integrating model is developed.

- Both the models suggest that the Molybdenum foil used in the modified XRF experiment was much too thick.

Chapter 6

Conclusion

The objective of my research was to optimise the per-pixel energy calibration technique of the MARS multi-energy scanner using the XRF technique discussed by Panta *et. al.*. The XRF energy calibration method used by Panta *et. al.* can be broken into two steps: (1) the fluorescence measurements and (2) using the fluorescence measurements to map the DAC steps to their energy response (keV). The main modification made to this method in this research was to measure the fluorescence photons found outside of the primary x-ray beam. This modification aimed to increase the ratio of fluorescence photons to background photons remaining from the polychromatic x-ray beam. Initial testing of the method, however, did not consistently detect the fluorescence for the molybdenum and tantalum foils. The XRF peaks were not well-defined and not consistent across the pixels. The lead XRF peak from the lead foil was clear and well-defined in each pixel.

Mo and Ta have relatively low atomic numbers and K_α values which means that they have low penetrability. In order for a maximum fluorescence signal to escape, the Mo and Ta foils must be thin. The Pb foil, on the other hand, has a much higher atomic number and K_α value and so a thicker foil is expected to absorb the higher energy x-rays. However, all of the foils in previous and modified XRF methods have foil thicknesses of 300 μm, regardless of their atomic number and K_α energies.

This led into an investigation for optimising the thickness of the foils used to ensure that maximum fluorescence is escaping the foil. Two stages of the model were developed: (1) the simple model for determining optimal foil thickness assumed a monochromatic beam and calculated the optimum foil thickness at the effective energy, (E_{Eff}), of the x-ray beam; and (2) the energy integrating model is a polychromatic model that used a numerical integration across all energies to give the foil thickness at which a maximum

fluorescence signal is detected. The results from the model suggest that E_{Eff} approximates a thicker foil than the optimum for the foils with lower energy. The models also confirm that the initial testing used sub-optimal foil thicknesses, explaining the low fluorescence signal in the initial experiments of the modified XRF method. The energy integrating model suggests a foil thickness of 50 μm for molybdenum, 100 μm for indium, and 210 μm for lead.

The optimal foil thickness model is being used to plan the next stage of experiments that the foil group will perform. The validity of the energy integrating model will be checked and the modified XRF technique described in this research will be automated so that minimal user intervention is required. Automating the energy calibration technique means that it will be easily implemented into the scanning procedure and the energy response of each pixel will be consistently known, giving improved image reconstruction and more accurate images.

Bibliography

[1] R Panta, M Walsh, S Bell, N Anderson, A Butler, and P Butler. Energy Calibration of the Pixels of Spectral X-ray Detectors. 2014.

[2] Raj Kumar Panta. *Toward human MARS scanning: improving spectral performance for soft tissue imaging.* PhD thesis, University of Otago".

[3] Adam M Alessio and Lawrence R MacDonald. Quantitative material characterization from multi-energy photon counting ct. *Medical physics*, 40(3):031108, 2013.

[4] William R Brody, Douglas M Cassel, F Graham Sommer, LA Lehmann, Albert Macovski, Robert E Alvarez, Norbert J Pelc, Stephen J Riederer, and Anne L Hall. Dual-energy projection radiography: initial clinical experience. *American Journal of Roentgenology*, 137(2):201–205, 1981.

[5] Dan Xu, David A Langan, Xiaoye Wu, Jed D Pack, Thomas M Benson, J Eric Tkaczky, and Andrea M Schmitz. Dual energy ct via fast kvp switching spectrum estimation. In *SPIE Medical Imaging*, pages 72583T–72583T. International Society for Optics and Photonics, 2009.

[6] NG Anderson, AP Butler, NJA Scott, NJ Cook, JS Butzer, N Schleich, M Firsching, R Grasset, N De Ruiter, M Campbell, et al. Spectroscopic (multi-energy) ct distinguishes iodine and barium contrast material in mice. *European radiology*, 20(9): 2126–2134, 2010.

[7] R Ballabriga, M Campbell, E Heijne, X Llopart, L Tlustos, and Winnie Wong. Medipix3: A 64k pixel detector readout chip working in single photon counting mode with improved spectrometric performance. *Nuclear Instruments and Methods in Physics Research Section A: Accelerators, Spectrometers, Detectors and Associated Equipment*, 633:S15–S18, 2011.

[8] Rafael Ballabriga, Jerome Alozy, G Blaj, M Campbell, M Fiederle, E Frojdh, EHM Heijne, Xavier Llopart, M Pichotka, Simon Procz, et al. The medipix3rx: a high resolution, zero dead-time pixel detector readout chip allowing spectroscopic imaging. *Journal of Instrumentation*, 8(02):C02016, 2013.

[9] Stephen Bell Philip Butler, Brian Goulter et al. Using Beer's law in MARS scanners. 2014.

[10] Kyra B Berg, James M Carr, Michael J Clark, Nick J Cook, Nigel G Anderson, Nicola J Scott, Al PM Butler, Philip H Butler, APH Butler, MARS-CT Team, et al. Pilot study to confirm that fat and liver can be distinguished by spectroscopic tissue response on a medipix-all-resolution system-ct (mars-ct). 2009.

[11] David P Cormode, Ewald Roessl, Axel Thran, Torjus Skajaa, Ronald E Gordon, Jens-Peter Schlomka, Valentin Fuster, Edward A Fisher, Willem JM Mulder, Roland Proksa, et al. Atherosclerotic plaque composition: Analysis with multicolor ct and targeted gold nanoparticles 1. *Radiology*, 256(3):774–782, 2010.

[12] E Roessl and R Proksa. K-edge imaging in x-ray computed tomography using multi-bin photon counting detectors. *Physics in medicine and biology*, 52(15):4679, 2007.

[13] R Aamir, A Chernoglazov, CJ Bateman, APH Butler, PH Butler, NG Anderson, ST Bell, RK Panta, JL Healy, JL Mohr, et al. Mars spectral molecular imaging of lamb tissue: data collection and image analysis. *Journal of Instrumentation*, 9(02): P02005, 2014.

[14] Faiz M Khan and John P Gibbons. *Khan's the Physics of Radiation Therapy*. Lippincott Williams & Wilkins, 2014.

[15] Jerrold T Bushberg and John M Boone. *The essential physics of medical imaging*. Lippincott Williams & Wilkins, 2011.

[16] Christopher James Bateman. *Methods for Material Discrimination in MARS Multi-Energy CT*. PhD thesis, University of Otago.

[17] Robert Cierniak. *X-ray computed tomography in biomedical engineering*. Springer Science & Business Media, 2011.

[18] J Anthony Seibert and John M Boone. X-ray imaging physics for nuclear medicine technologists. part 2: X-ray interactions and image formation. *Journal of nuclear medicine technology*, 33(1):3–18, 2005.

[19] NG Anderson, AP Butler, NJA Scott, NJ Cook, JS Butzer, N Schleich, M Firsching, R Grasset, N De Ruiter, M Campbell, et al. Spectroscopic (multi-energy) ct distinguishes iodine and barium contrast material in mice. *European radiology*, 20(9): 2126–2134, 2010.

[20] James Ambrose. Computerized transverse axial scanning (tomography): Part 2. clinical application*. *The British journal of radiology*, 46(552):1023–1047, 1973.

[21] Richard A Robb. X-ray computed tomography: from basic principles to applications. *Annual review of biophysics and bioengineering*, 11(1):177–201, 1982.

[22] Taly Gilat Schmidt. Optimal ?image-based? weighting for energy-resolved ct. *Medical physics*, 36(7):3018–3027, 2009.

[23] Robert E Alvarez and Albert Macovski. Energy-selective reconstructions in x-ray computerised tomography. *Physics in medicine and biology*, 21(5):733, 1976.

[24] Jan Jakubek. Data processing and image reconstruction methods for pixel detectors. *Nuclear Instruments and Methods in Physics Research Section A: Accelerators, Spectrometers, Detectors and Associated Equipment*, 576(1):223–234, 2007.

[25] Katsuyuki Taguchi, Mengxi Zhang, Eric C Frey, Xiaolan Wang, Jan S Iwanczyk, Einar Nygard, Neal E Hartsough, Benjamin MW Tsui, and William C Barber. Modeling the performance of a photon counting x-ray detector for ct: Energy response and pulse pileup effects. *Medical physics*, 38(2):1089–1102, 2011.

[26] S Kappler, D Niederlöhner, K Stierstorfer, and T Flohr. Contrast-enhancement, image noise, and dual-energy simulations for quantum-counting clinical ct. In *SPIE Medical Imaging*, pages 76223H–76223H. International Society for Optics and Photonics, 2010.

[27] Björn J Heismann, Bernhard T Schmidt, and Thomas Flohr. Spectral computed tomography. SPIE, 2012.

[28] H Zeller, S Dufreneix, M Clark, PH Butler, APH Butler, N Cook, and L Tlustos. Charge sharing between pixels in the spectral medipix2 x-ray detector. In *Image and Vision Computing New Zealand, 2009. IVCNZ'09. 24th International Conference*, pages 363–366. IEEE, 2009.

[29] C Schwarz, M Campbell, R Goeppert, EHM Heijne, J Ludwig, G Meddeler, B Mikulec, E Pernigotti, M Rogalla, K Runge, et al. X-ray imaging using a hybrid photon counting gaas pixel detector. *Nuclear Physics B-Proceedings Supplements*, 78(1):491–496, 1999.

[30] TR Melzer, NJ Cook, AP Butler, R Watts, N Anderson, R Tipples, and PH Butler. Spectroscopic biomedical imaging with the medipix2 detector. *Australasian Physics & Engineering Sciences in Medicine*, 31(4):300–306, 2008.

[31] Rafael Ballabriga, Jerome Alozy, G Blaj, M Campbell, M Fiederle, E Frojdh, EHM Heijne, Xavier Llopart, M Pichotka, Simon Procz, et al. The medipix3rx: a high resolution, zero dead-time pixel detector readout chip allowing spectroscopic imaging. *Journal of Instrumentation*, 8(02):C02016, 2013.

[32] Rafael Ballabriga, Jerome Alozy, G Blaj, M Campbell, M Fiederle, E Frojdh, EHM Heijne, Xavier Llopart, M Pichotka, Simon Procz, et al. The medipix3rx: a high resolution, zero dead-time pixel detector readout chip allowing spectroscopic imaging. *Journal of Instrumentation*, 8(02):C02016, 2013.

[33] Rafidah Binti Zainon. Spectral micro-ct imaging of ex vivo atherosclerotic plaque. 2012.

[34] Rafael Ballabriga, Jerome Alozy, G Blaj, M Campbell, M Fiederle, E Frojdh, EHM Heijne, Xavier Llopart, M Pichotka, Simon Procz, et al. The medipix3rx: a high resolution, zero dead-time pixel detector readout chip allowing spectroscopic imaging. *Journal of Instrumentation*, 8(02):C02016, 2013.

[35] Marcel JM Pelgrom, Aad CJ Duinmaijer, Anton PG Welbers, et al. Matching properties of mos transistors. *IEEE Journal of solid-state circuits*, 24(5):1433–1439, 1989.

[36] Anatoily Manuilskiy, Börje Norlin, Hans-Erik Nilsson, and Christer Fröjdh. Spectroscopy applications for the medipix photon counting x-ray system. *Nuclear Instruments and Methods in Physics Research Section A: Accelerators, Spectrometers, Detectors and Associated Equipment*, 531(1):251–257, 2004.

[37] Thomas Koenig, Marcus Zuber, Elias Hamann, Angelica Cecilia, Rafael Ballabriga, Michael Campbell, Marie Ruat, Lukas Tlustos, Alex Fauler, Michael Fiederle, et al. How spectroscopic x-ray imaging benefits from inter-pixel communication. *Physics in medicine and biology*, 59(20):6195, 2014.

[38] S. Kaczmarz. Angen ad?herte auflausung von systemen linearer gleichungen. *e l?Acad Al?mie Polonaise des Sciences et des Lettres. Classe des Sciences Math Al?matiques et Naturelles. S Al?rie A, Sciences Math Al?matiques,*, 35:355–357, 1937.

[39] Nate D Tang, Niels De Ruiter, JL Mohr, Anthony PH Butler, Philip H Butler, and R Aamir. Using algebraic reconstruction in computed tomography. In *Proceedings of the 27th Conference on Image and Vision Computing New Zealand*, pages 216–221. ACM, 2012.

[40] Julia F Barrett and Nicholas Keat. Artifacts in ct: Recognition and avoidance 1. *Radiographics*, 24(6):1679–1691, 2004.

[41] K Rajendran, MF Walsh, NJA de Ruiter, AI Chernoglazov, RK Panta, APH Butler, PH Butler, ST Bell, NG Anderson, TBF Woodfield, et al. Reducing beam hardening effects and metal artefacts in spectral ct using medipix3rx. *Journal of Instrumentation*, 9(03):P03015, 2014.

[42] Clemens Maaß, Esther Meyer, and Marc Kachelrieß. Exact dual energy material decomposition from inconsistent rays (mdir). *Medical physics*, 38(2):691–700, 2011.

[43] Kwang Eun Jang, Jongha Lee, Younghun Sung, and SeongDeok Lee. Information-theoretic discrepancy based iterative reconstructions (idir) for polychromatic x-ray tomography. *Medical physics*, 40(9):091908, 2013.

[44] Ruoqiao Zhang, J-B Thibault, Charles A Bouman, Ken D Sauer, and Jiang Hsieh. Model-based iterative reconstruction for dual-energy x-ray ct using a joint quadratic likelihood model. *Medical Imaging, IEEE Transactions on*, 33(1):117–134, 2014.

[45] Thomas König. Exploring coherent phenomena and energy discrimination in x-ray imaging. 2011.

[46] Thomas Koenig, Julia Schulze, Marcus Zuber, Kristian Rink, Jochen Butzer, Elias Hamann, Angelica Cecilia, Andreas Zwerger, Alex Fauler, Michael Fiederle, et al. Imaging properties of small-pixel spectroscopic x-ray detectors based on cadmium telluride sensors. *Physics in medicine and biology*, 57(21):6743, 2012.

[47] C Ponchut, JL Visschers, A Fornaini, H Graafsma, M Maiorino, G Mettivier, and D Calvet. Evaluation of a photon-counting hybrid pixel detector array with a synchrotron x-ray source. *Nuclear Instruments and Methods in Physics Research Section A: Accelerators, Spectrometers, Detectors and Associated Equipment*, 484 (1):396–406, 2002.

[48] EN Gimenez, R Ballabriga, M Campbell, I Horswell, X Llopart, J Marchal, KJS Sawhney, N Tartoni, and D Turecek. Study of charge-sharing in medipix3 using a micro-focused synchrotron beam. *Journal of Instrumentation*, 6(01):C01031, 2011.

[49] R Ballabriga, M Campbell, E Heijne, X Llopart, L Tlustos, and Winnie Wong. Medipix3: A 64k pixel detector readout chip working in single photon counting mode with improved spectrometric performance. *Nuclear Instruments and Methods in Physics Research Section A: Accelerators, Spectrometers, Detectors and Associated Equipment*, 633:S15–S18, 2011.

[50] JP Ronaldson, M Walsh, SJ Nik, J Donaldson, RMN Doesburg, D van Leeuwen, R Ballabriga, MN Clyne, APH Butler, and PH Butler. Characterization of medipix3 with the mars readout and software. *Journal of Instrumentation*, 6(01):C01056, 2011.

[51] Dermott Edward Cullen, MH Chen, JH Hubbell, ST Perkins, EF Plechaty, JA Rathkopf, and JH Scofield. Tables and graphs of photon-interaction cross sections from 10 ev to 100 gev derived from the llnl evaluated photon data library (epdl). Technical report, Lawrence Livermore National Lab., CA (USA), 1989.

[52] RW Fink, RC Jopson, Hans Mark, and CD Swift. Atomic fluorescence yields. *Reviews of Modern Physics*, 38(3):513, 1966.

[53] Walter Bambynek, Bernd Crasemann, RW Fink, H-U Freund, Hans Mark, CD Swift, RE Price, and P Venugopala Rao. X-ray fluorescence yields, auger, and coster-kronig transition probabilities. *Reviews of Modern Physics*, 44(4):716, 1972.

[54] JH Hubbell, Wm J Veigele, EA Briggs, RT Brown, DT Cromer, and RJ Howerton. Atomic form factors, incoherent scattering functions, and photon scattering cross sections. *Journal of physical and chemical reference data*, 4(3):471–538, 1975.

[55] Charles Glover Barkla. X-rays and the theory of radiation. *Journal of the Röntgen Society*, 14(55):73–73, 1918.

[56] James H Scofield. Theoretical photoionization cross sections from 1 to 1500 kev. Technical report, California Univ., Livermore (USA). Lawrence Livermore Lab, 1973.

[57] Martin J Berger, JH Hubbell, SM Seltzer, J Chang, JS Coursey, R Sukumar, DS Zucker, and K Olsen. Xcom: photon cross sections database. *NIST Standard reference database*, 8(1):3587–3597, 1998.

[58] J Alles and RF Mudde. Beam hardening: Analytical considerations of the effective attenuation coefficient of x-ray tomography. *Medical physics*, 34(7):2882–2889, 2007.